POLITECNICO DI TORINO

Master degree in Energetic and Nuclear Engineering

Master thesis

Engineering self-heated micro-reformer for micro-solid oxide fuel cell applications

Institut de Recerca en Energia de Catalunya
Catalonia Institute for Energy Research

Tutor

Prof. Federico Smeacetto

Prof. Monica Ferraris

Supervisor

Dr. Francesco Chiabrera

Dr. Nerea Alayo

Dr. Marco Bianchini

Candidate

Roberto Maniaci

20 March 2020

Abstract

The relevance of portable electronic devices has increased constantly in the lasts years leading to a growing interest in more efficient portable power sources. Among the proposed solutions, micro-solid oxide fuel cell power generators (μ-SOFC PG) are one of the most interesting alternatives to traditional Li batteries, due to their superior energy and power density, long lifetime and high reliability. μ-SOFC shares the same working principles of traditional SOFC, but the entire cell is based on thin films, drastically reducing the ohmic losses and allowing to operate at temperatures below 600 °C. Moreover, the system is integrated in Si technology, offering the possibility of using mainstream fabrication processes of Micro Electro-Mechanical Systems (MEMS) and, therefore, assuring low cost and a facile scale up to large scale production. One of the most important components of the μ-SOFC system is the fuel processing unit (μ-reformer), which allows working with liquid hydrocarbons fuels (Dimethyl Ether in this work), drastically increasing the energy density of the entire device. Nevertheless, some important issues related with fast start-up, stand-alone reforming of the fuel and low power consumption still need to be faced for allowing a reliable and effective integration into the μ-SOFC system. This thesis is devoted to improve this silicon based fuel processing unit, both by numerical modelling and by the fabrication and testing of a self-heated μ-reformer.

The Si-based μ-reformer is integrated in a 1x1 cm^2 Si substrate of 500 μm of thickness. The active part of the μ-reformer is composed by a micro-fabricated suspended platform, in which an array of more than 6000 microchannels and a metallic heater are located, which is intended to provide the thermal power necessary for the fuel processing. The microchannels (50 μm of diameter) are covered with two different catalysts, γ-phase alumina and platinum, which are expected to reform the hydrocarbons into hydrogen. After having followed the main fabrication steps of the Si-based μ-reformer, the deposition of these catalysts was successfully carried out by Atomic Layer Deposition (ALD). The thermal behaviour of the self-heated μ-reformers was then characterized by Raman in-situ measurements of the sample's temperature as a function of the electrical power supplied. In this way, by following the shift of the main Si Raman mode, an estimation of the device temperature as function of the ohmic resistance of the heater was founded, also confirmed by a thermal FEM model. The devices show a fast start-up and a maximum temperature of 600 °C in vacuum, which is limited by the thermal losses from the suspended platform towards the Si substrate. After the thermal characterization of the substrate, the catalytic properties of these self-heated devices were assessed by feeding dimethyl ether and air to the μ-reformers and measuring the reformed gas flow by a micro-gas chromatography (μ-GC). The results showed that hydrogen was successfully produced by the self-heated μ-reformer but the percentage of conversion appeared to be low, probably due to a scarce Pt coverage of the device. Finally, a Finite Element Method (FEM) model of one microchannel has been developed in order to reproduce and improve the obtained results. The simulations showed a good match with previously obtained experimental results as a function of the μ-reformer's temperature. An optimization analysis was carried out by varying some geometrical and physical parameters, offering important insights for the design and manufacturing of the next generation of μ-reformers for μ-SOFC technology.

INDEX

Figures list 6

Tables list 7

1 INTRODUCTION 1

1.1 Increasing demand of portable devices 1

1.2 Limits and problems of nowadays technology 2

1.3 µ-SOFC as solution..2

1.4 State of the art µ-fuel cell 4

1.4.1 Materials and working principle 4

1.4.2 Fuel reformer 6

1.4.3 Problems and challenging..8

1.5 Scope of the thesis 9

2 Experimental Methods 10

2.1 Microfabrication..10

2.1.1 Thin film deposition..10

2.1.2 Photolithography 10

2.1.3 Etching 11

2.2 Calibration of suspended µ-reformer by Raman spectroscopy..............11

2.2.1 Raman spectroscopy 11

2.2.2 In-situ Raman spectroscopy..13

2.3 Catalyst deposition and characterization 13

2.3.1 Atomic Layer Deposition (ALD) 13

2.3.2 Rapid Thermal Processing (RTP) 14

2.3.3 Ellipsometry 15

2.3.4 Scanning Electron Microscope (SEM)..15

2.3.5 Energy dispersive X-Ray Spectroscopy (EDX) 16

2.4 Analysis of reformed flow..17

2.4.1 Micro-gas chromatography (µ-GC) 17

2.5 Finite Element Method (FEM)..17

3 Microfabrication of µ-reformer 19

3.1 Suspended µ-reformer 19

3.1.1 Design 19

3.1.2 Microfabrication steps 20

3.1.3 Functionalization 21
4 Testing and calibration of self-heated µ-reformer for fast start-up 23
4.1 Introduction 23
4.2 Calibration of the heater 23
4.2.1 Set-up 23
4.2.2 Results 24
4.3 Thermal evaluation 27
4.3.1 Experimental results 27
4.3.2 Simulation model 28
4.3.3 Thermal optimization 31
4.4 Chemical evaluation 32
4.4.1 Experimental set-up 32
4.4.2 DME partial oxidation 34
4.4.3 Results 34
5 Understanding the performances of steady-state µ-reformer 37
5.1 Introduction 37
5.1.1 Description of set-up 37
5.1.2 DME steam reforming 38
5.2 Simulation model 39
5.2.1 Geometry and mesh 39
5.2.2 Physics 41
5.2.3 Results 46
5.3 Optimization 56
5.3.1 Chosen parameter 56
5.3.2 Result 57
6 Conclusions 64

FIGURES LIST

Figure 1-Trend of portable devices market 2012-2020 (https://www.grandviewresearch.com)..........1
Figure 2- Energy density micro-SOFC [6]..3
Figure 3- System layout of μ-SOFC PG 4
Figure 4- TPB schematic (Carlos Lòpez-Gàndara et al., Journal of Sensors Volume 2009, Article ID 258489) 5
Figure 5- working principle of SOFC (https://mypages.iit.edu)...6
Figure 6-Working principle of an External micro-reformer 7
Figure 7-Encapsulation schematic [18] 8
Figure 8- Schematic procedure of photolithography (https://static1.squarespace.com) 11
Figure 9- Scattering of light (https://www.nanophoton.net) 12
Figure 10- Working principle (http://cnx.org/) 12
Figure 11-Linkam stage and controller (www.linkam.co.uk) 13
Figure 12- ALD deposition [19] 14
Figure 13- Ellipsometry working principle [20] 15
Figure 14- Schematic of basic SEM components (https://study.com)...16
Figure 15- micro-GC schematic (Wikipedia)..17
Figure 16- Suspended u-reformer [18] 19
Figure 17- a) SEM image of cross section of the suspended u-reformer b) microscope image of the suspended u-reformer 20
Figure 18- Schematic cross section of heater...20
Figure 19- Fabrication steps of u-reformer [18] 21
Figure 20- Alumina pillars. SEM image of the sample cross section 22
Figure 21-Experimental set-up for in-situ Raman 24
Figure 22- Raman shift for different input power 25
Figure 23- Reference for the conversion in temperature of the Raman Shift [26] 25
Figure 24- Calibration curves of the heater 26
Figure 25- Detail while the calibration was carried out..27
Figure 26- Domain (a) and mesh (b) of the thermal simulation..28
Figure 27- Thermal model conditions...29
Figure 28- Temperature distribution with 5.5 W 30
Figure 29-Temperature distribution with 5.5 W with only the 300 nm Si_3N_4 layer............................31
Figure 30- Heat dissipation comparison between the non-optimized and optimized configuration ...32
Figure 31- Experimental set-up 33
Figure 32- a) new sample b) heater after ALD depostion of alumina c) heater after ALD depositon of Pt 35
Figure 33-a) confocal microscope images of the heater after RTP b),c) SEM images of the heater after RTP 36
Figure 34- Set-up of steady state experiment...38
Figure 35-Geometry of the model...40
Figure 36- Mesh of the geometry..40
Figure 37-Site of the reactions 43
Figure 38- Velocity field 47
Figure 39- Temperature distribution 48
Figure 40- concentration of hydrogen and DME 49

Figure 41- Rate of reaction of hydrogen 49
Figure 42- DME conversion comparison 50
Figure 43- Hydrogen percentage comparison....51
Figure 44-CO,CO_2,CH_4 conversion comparison....52
Figure 45- Composition of exiting flow....53
Figure 46-Error evaluation colour ma....55
Figure 47- Grid independence....56
Figure 48- Length dependence for DME conversion 57
Figure 49- Length dependence for hydrogen production....58
Figure 50- Radius dependence for DME conversion....59
Figure 51- Radius dependence for hydrogen production 59
Figure 52- Flow rate dependence for DME conversion 60
Figure 53-Flow rate dependence for hydrogen production....61
Figure 54- Power evaluation 62
Figure 55- DME/steam ratio comparison for H_2 production....62

TABLES LIST

Table 1- Map of the temperature....28
Table 2- Comparison between model and experimental results 30
Table 3-Comparison between original case and optimized case 32
Table 4-Result of the µ-GC 35
Table 5- Activation energies....43
Table 6- Reactions rates....44
Table 7- Entering flow rate and concentration 45
Table 8 - Average error evaluation 54
Table 9- Optimization parameters....56
Table 10- Molar Gibbs free energies....61
Table 11-H2 production in function of DME/steam ratio 63

1 INTRODUCTION

1.1 INCREASING DEMAND OF PORTABLE DEVICES

The demand of energy is growing day by day due to increasing industrialization and population, but mostly there is an increasing demand for clean energy in order to avoid rising greenhouse gases emission, which results as one of the main issues for the climatic emergency.

Industries are changing significantly the way of production due to the advent of the portable electronics demand. Portable electronic is basically referred to the held hand device. The key factor of the global changing and what is expect to be the main protagonist is the smartphone proliferation. In general, the driving factor of the technological development is the need of smart portable devices (i.e. tablets, notebooks, smartphones) [1]. Figure 1 shows the trend of the demand. In the y axis is reported the number of million devices. The highest percentage is represented by the smartphones, but also the tablets demand is increasing. However, the overall trend is hugely increasing, as nowadays the number of devices is more than double with respect to 2012.

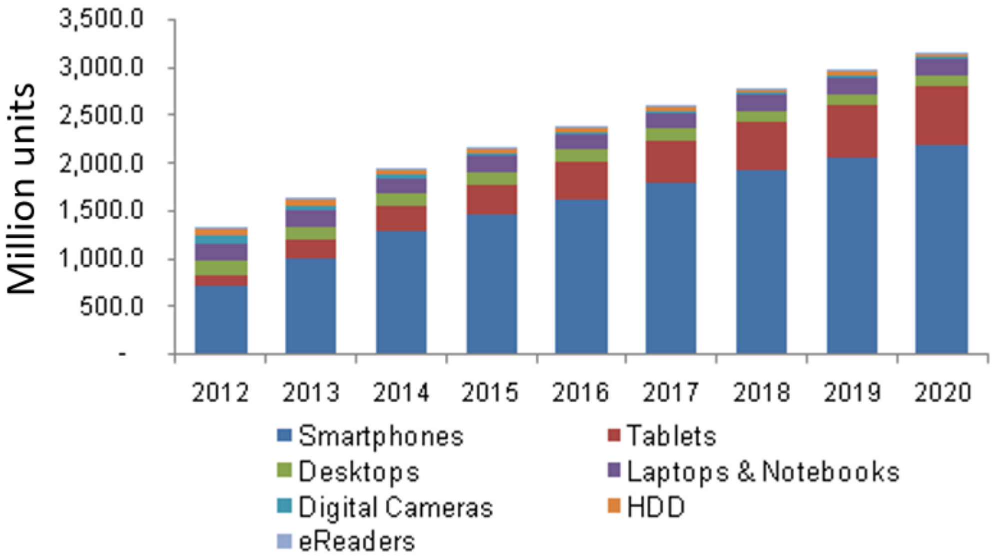

Figure 1-Trend of portable devices market 2012-2020 (https://www.grandviewresearch.com)

Today the smart devices play an important role in the business of everyday life, this lead to an increase of interest in the battery life and efficiency highlighting the limit and problem of the nowadays used technologies. The interest in new technologies for supply the power to these devices in a reliable way has increase in the las t years. The trend is to enhance the performances of the portable electronics (i.e. audio, video, high performance processor, longer battery lifetime) in order to offer a complete device able to help and make more comfortable the everyday life.

1.2 LIMITS AND PROBLEMS OF NOWADAYS TECHNOLOGY

The most common device for supply the power to the portable electronics is the Li ion battery. It is a rechargeable battery and it is based on the movement on the lithium ions. This battery produces electricity by the movement of the lithium ions from the negative electrode to the positive electrode passing through an electrolyte. The lithium atoms are ionized in the negative electrode and separated from the electrons. After passing through a electrolyte, the atoms recombines with the electrons in the positive electrode. The electrons pass through an external path producing electricity. During the charging process the movement of the ions is the opposite and the power is supplied to the battery. However, even if is the most used power supplier for the portable devices, there are some limitations that shifted the research towards other technologies. The main limitations are[2], [3]:

- The most of Li ion batteries uses a flammable electrolyte that can lead to an explosion if the battery is damaged or if it is not charged in the correct way. Thus, for safety reasons, it is required a safety mechanism that can increase the weight and limit the performances.
- The manufacturing cost is elevated if compared with the other batteries.
- The maximum value of the current in charge or discharge process cannot exceed 2C for safety reasons.
- Aging is a relevant problem. The capacity of the batteries is degraded even if not used.
- High temperature is also a problem for safety and aging reasons. If stored in a warm ambient, the degradation process is favoured.
- Due to self-discharging, the charging percentage if the battery is reduced even if not used.

These are the main problems that have raised interest for other more efficient and more reliable power supplier.

1.3 μ-SOFC AS SOLUTION

One of the most attractive candidates for replacing the current technologies for power supply is doubtless the μ-Solid Oxide Fuel Cell. This technology uses the same working principle of the classical bulk SOFC, the substantial difference lies in the use of thin film membrane. The miniaturization of the device allows to reduce the dimension and also the thermal inertia allowing a fast start-up making the device compatible for dynamic operations, one of the most penalizing drawbacks of the bulk SOFC. Moreover, thanks to the reduced thickness of the electrolyte (even below 500 nm), the ohmic drop across the electrodes decreased significantly leading to an operating temperature of the device even lower than 500 °C [4]. This is an important result if compared to the normal operating temperature of the bulk device that is even higher than 900 °C. Another important characteristic is the high energy density [5]. By comparing the different power suppliers (Figure 2), is clear that the μ-SOFCs are characterized by the highest energy density among them[6].

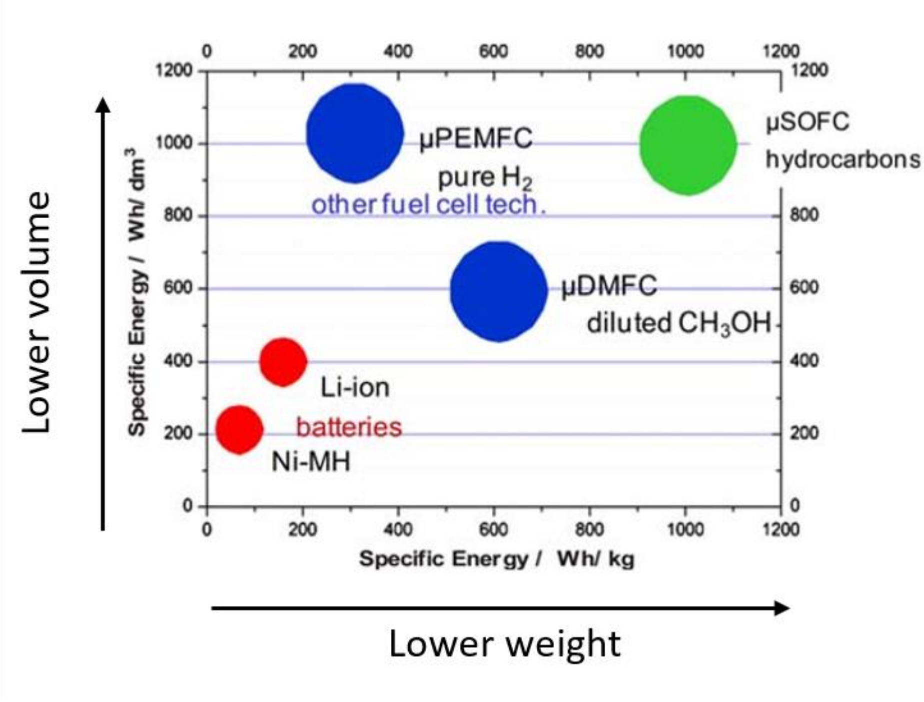

Figure 2- Energy density micro-SOFC [6]

Compared with the other types of cell, it can be fed with different type of fuel, especially if deriving from biomass. Clearly the cell operates with higher efficiency if fed with pure hydrogen, but good result can be achieved also with different fuels (i.e. methanol, propane, DME).

Another important advantage is that the Si-based µ-SOFCs are Microelectromechanical systems (MEMS), miniaturized mechanical and electro-mechanical elements realized by microfabrication process. The already affirmed microfabrication techniques based on Silicon allow a mass production and cost effective fabrication process. However, in order to form a complete µ-SOFC Power Generator (PG) it is necessary a fuel cell stack comprising additional components as: a fuel processing unit for hydrogen production from the hydrocarbon fuel, a post-combustor unit for processing the exhaust gases and a heat management unit [7], [8]. The fuel and the air (or steam) are injected separately inside the fuel processing unit, also called µ-reformer. The two flows are heated-up to ensure a gaseous phase and are converted by the µ-reformer in molecules (i.e. H_2, CO, CO_2). Usually the conversion reaction is catalysed and depending on the catalyst used there are different side products (i.e. MeOH, CH_4) . Then air is pre-heated and fed to the cathode of the cell where reacts with the reformed hydrogen to produce electrical power. If present, the unreacted fuel mixes with air and is burned in the post combustor unit. In this way, clean exhaust gases leave the system. A possible system layout is shown in Figure 3. In the figure are also represented the interconnectors. They are made on a particular alloy in order to ensure a good electrical conductivity at operating temperature, a good oxidation resistance for long time and a similar coefficient of thermal expansion of the electrolyte material (Yttria Stabilized Zirconia, YSZ)[9].

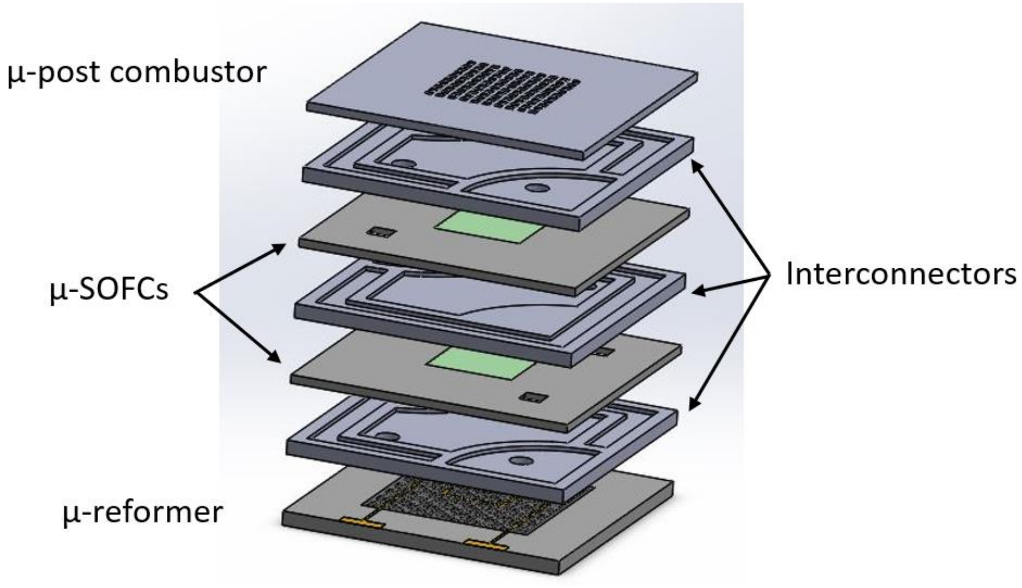

Figure 3- System layout of μ-SOFC PG

1.4 STATE OF THE ART μ-FUEL CELL

1.4.1 Materials and working principle

Solid oxide fuel cells (SOFC) are composed of two electrodes (anode and cathode) and an electrolyte. The electrolyte, allows the passage of the oxygen ions from the cathode to the anode causing a difference of voltage between the electrodes that lead to the generation of a current through an external load. To fulfil this role is required: a high ionic conductivity and a very low (near to zero) electronic conductivity, a thermal expansion compatible with those of the others components of the cell a good resistance to thermal cycling and a good chemical and thermal stability. The most used electrolyte in the state of the is Yttria Stabilized Zirconia (YSZ) [10], [11]. YSZ is one of the today's most used slid oxide electrolyte material and its characteristics are well known. Generally, high temperature are needed for using this type of electrolyte, but, by reducing significantly the thickness to thin films (even below the μm), the operating temperature is drastically reduced. The most common methods for depositing a thin film layer of electrolyte are Pulse Laser Deposition (PLD), Atomic Layer Deposition (ALD) and Chemical Vapour Deposition (CVD). The objective of the deposition is to obtain a dense and homogeneous layer trying to avoid formation of pinholes that can lead to the failure of the cell.

The electrodes play also an important role for achieving good performances. They are involved in the oxidation and reduction reactions and are responsible to collect the current. Some requirements are the same for both electrodes. First of all, it is needed the use of highly porous thin film in order to facilitate the mass transport. Also in this case the thermal expansion coefficient has to be compatible with the other components and is required a good resistance for thermal cycling and a good chemical stability. Furthermore, a high catalytic activity is fundamental to run the system. Unlike the electrolyte, for these components a high electronic conductivity is needed for a better current collection. Also a good ionic conductivity is required, in fact are often used MIEC (mixed ionic electronic conductors) materials. In particular, in the anode the connection between the metal (catalyst), the electrolyte and the gas phase is named triple phase boundary (TPB), shown in Figure 4. For a good TPB working it is necessary to have access to hydrogen from the fuel inlet, have access to the oxygens ions transported by the YSZ electrolyte and be able to transport electrons towards the external load. As more porous is the layer as much better the TPB works [12].

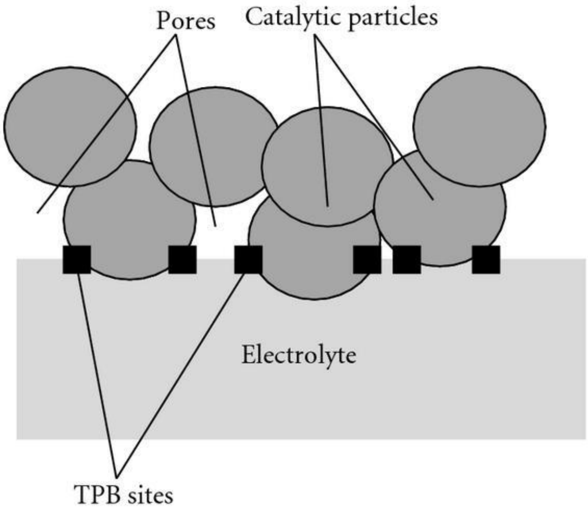

Figure 4- TPB schematic (Carlos Lòpez-Gàndara et al., Journal of Sensors Volume 2009, Article ID 258489)

The most used electrodes in µ-SOFCs are platinum thin films [7], [13]. Platinum is a pure electronic conductor and can be deposited by thermal evaporation obtaining a dense layer of material. However is necessary to perform a thermal treatment in order to reach the desired porosity. In the case of electrodes, the used material are different from the bulk devices due to the lower operational temperature. In fact, nickel catalyst cannot be used even if cheaper the platinum.

As mentioned before, the µ-SOFC shares the same working principle of the bulk SOFC. The schematic is reported in Figure 5. For simplicity only hydrogen is shown as fuel, but also methane ad carbon monoxide can be converted in electricity. The hydrogen is fed to the anode side and, reacting with the oxygen ions transported from the electrolyte, forms water and 2 electrons. The chemical reaction involved is:

$$H_2 + O^{2-} = H_2O + 2e^-$$

Water exits the system, while electrons passes through an external circuit producing a current that supply a ohmic load. Then the electrons reach the cathode where they are recombined with the fed oxygen in order to ionizes it and produces the O^{2-} ions that will migrate to the anode to repeat the process. The reaction involved in the cathode is:

$$O_2 + 4e^- = 2O^{2-}$$

While the overall reaction is:

$$\frac{1}{2}H_2 + O_2 = H_2O + \ \Delta E$$

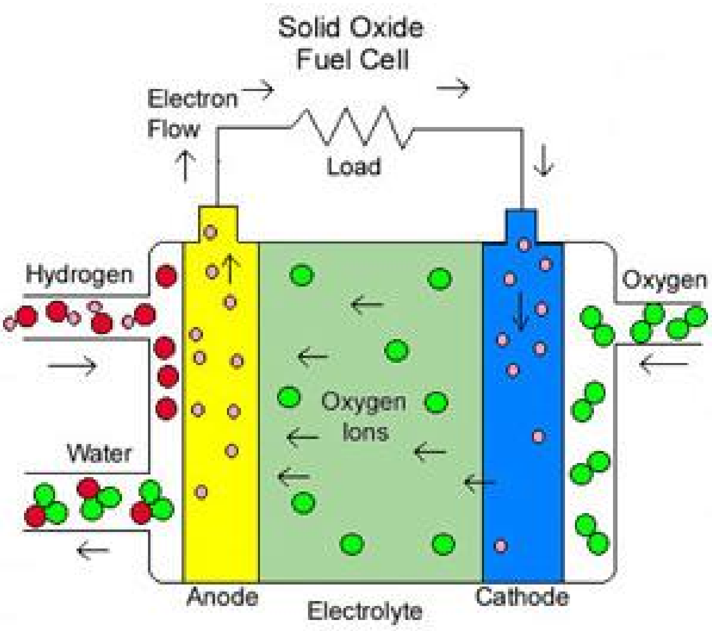

Figure 5- working principle of SOFC (https://mypages.iit.edu)

However is not easy to find hydrogen as pure element in nature. Thus, it is necessary to produce it. The fuel processing unit, or reformer, play this important role.

1.4.2 Fuel reformer

An ideal condition would be fed the cell directly with the pure hydrogen. Since the hydrogen is not present in the atmosphere as elemental form and however would be very tricky to store it safely, the aim of the reformer is to convert the entering gas into pure hydrogen in order to be used inside the cell as fuel.

Short-Chain hydrocarbons are preferred because are safe to handle and they are available in the market. Methane, Bio-gas, Syngas, dimethyl ether can be used as fuel. According to the today's challenge of develop a clean and sustainable process for producing electrical energy, fuel flexibility plays a crucial role for achieving this objective [14]. Among the various possible fuels, dimethyl ether (DME) is one of the most attractive. The high content of H_2 (around 13 wt%) and also the possibility to use the already existent LPG infrastructures for handle and store the fuel have increased the interest in using DME as fuel. It is non-carcinogenic, non-corrosive and non-toxic fuel and, furthermore, can be easily synthetized by natural gas, coal, biomass. Dimethyl ether also removes the dependency on liquefied petroleum gases that are currently used. It also can be used as a diesel substitute for the similar characteristics, and this would decrease NOx, SOx, and particulate matter emissions. Additional research includes dimethyl ether steam reforming and partial oxidation to produce hydrogen-rich fuel-cell feeds [15].

It is possible to have internal or external reforming. In the first case the gas is directly converted inside the cell, precisely in the anode. In the most of the cases the reforming reactions are endothermic and this can play a cooling role for the SOFC system. Another advantage is the possibility to avoid an further component inside the system making it simpler and more efficient. However, this would generate a inhomogeneous temperature distribution inducing mechanical and thermal stress that may lead to the failure of the cell [16]. While, in the external reforming the reactions take place inside another unit located just before the cell, thus not affecting the temperature distribution as the previous case. However, it is necessary to adopt a more complex design of the system including a good thermal management.

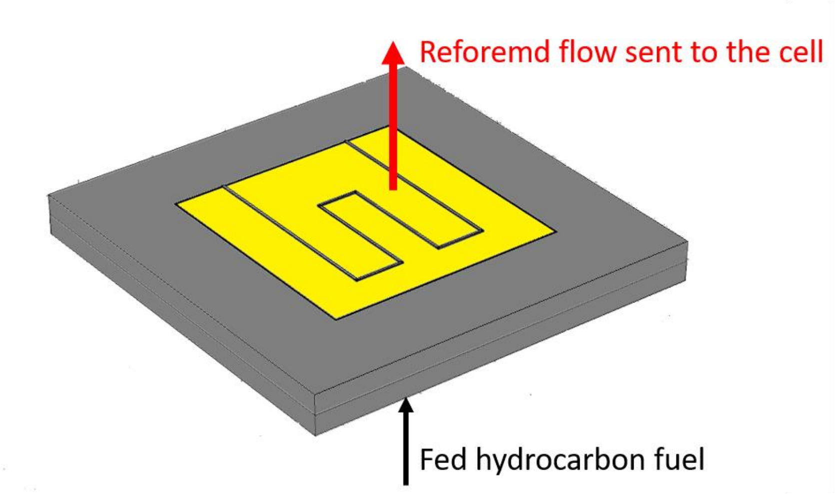

Figure 6-Working principle of an External micro-reformer

Usually the reforming reactions are helped by the presence of catalysts. The catalysts reduce the activation energy of the chemical reaction leading to a higher conversion efficiency. The type of catalyst depends on the type of reaction involved. There many types of reforming processes such as dry reforming, steam reforming, auto-thermal reforming, partial-oxidation reforming. One of the most common reforming reaction is methane steam reforming:

$$CH_4 + H_2O = CO + 3H_2$$

$$CO + H_2O = CO_2 + H_2$$

Due to the formation of CO from the first reaction, Water-Gas Shift takes also place and leads to a supplementary conversion in H_2. The overall steam methane reforming reaction:

$$CH_4 + 2\,H_2O = CO_2 + 4\,H_2$$

However, the reforming unit can be also used with the only aim of hydrogen production. In a possible future where the hydrogen plays a central role as fuel for green-electricity production, this component can also be developed and improved pursing this scope.

1.4.3 Problems and challenging

Since μ-SOFC is a developing technology, it is characterized by some problems and challenging. Fast start-up and shut-down are a key factors for this devices. The start-up process usually involves exothermic reactions (i.e. partial oxidation or complete oxidation) as heat source for reach the operating as fast as possible. They are supposed to supply power in dynamic conditions, with sudden and unpredictable changes in load. For pursuing this objective is also required a low thermal mass. The operating temperature (300-600°C) can be a problem due to the different thermal expansion of the different thin film composing the cell. As ceramics thin films and Si-based substrate are characterized by different coefficients, this could reduce the mechanical stability of the membrane due to the mechanical stress generated in the interface of the different materials [17]. Another important challenge is to achieve a good percentage of conversion by the μ-reformer with a high selectivity for hydrogen. By lowering the operating temperature, the coke deposition could be a relevant problem for the deactivation of the catalyst.. The thermal management of the device is also a relevant factor [6]. For encapsulate the cell in a proper manner (a possible set-up is shown in Figure 7), the thermal management is fundamental. The huge temperature difference between the hot system (around 600°C) and the exterior handling temperature required a good insulation and efficient heat exchange.

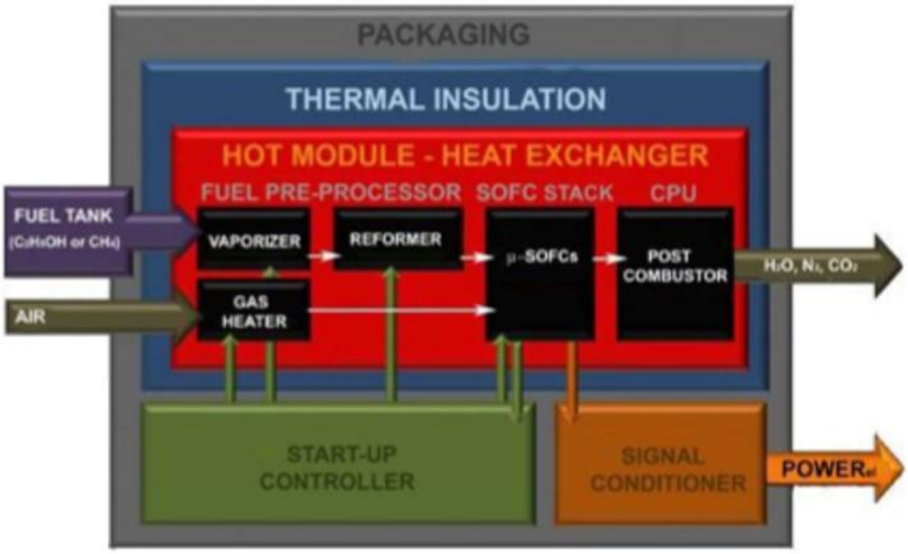

Figure 7-Encapsulation schematic [18]

Finally, it is also under development the choice of the electrolyte and electrodes materials to maximize the performances of the system.

1.5 SCOPE OF THE THESIS

This work is devoted to improve the silicon based fuel processing unit for the presented µ -SOFC, both by numerical modelling and by the fabrication and testing of a self-heated µ-reformer. The study is focused on the two working conditions of the device: start-up and steady state. In details, the thesis deal with the characterization of the µ-heater of this device and the further experimental test for the evaluation of the conversion efficiency of the fuel (Dimethyl Ether in this work) in hydrogen and also of the effective fast start-up process. The device is also functionalized with proper catalysts. It is also performed a thermal assessment and model simulation of a possible optimization for improve the insulation of the central active area. Regarding the steady state condition, a FEM model is implemented, based on experimental data, in order to simulate an optimization for eventually improvement in manufacturing new and more efficient technologies. The optimization is based on the variation of geometrical and physical parameter with the scope of find a configuration that lead to an increment of the DME conversion efficiency and hydrogen production.

The thesis is organized as follow:

- **Chapter 2** describes all the experimental techniques used for characterize, test, functionalize the sample with the relative parameters used in this work. It also describes the FEM method on which are based all the simulation model implemented in the work.
- **Chapter 3** presents the microfabrication and design of the µ-reformer. The design of the sample is explained in detail and the microfabrication steps that lead to the final device are summed up. The scope of this chapter is purely descriptive since the samples were already manufactured due to the long-lasting manufacturing process.
- **Chapter 4** deals with the start-up condition of the device. The µ-heater is well characterized and is performed a chemical experiment to evaluate the efficiency of the self-heated set-up. Also a thermal optimization is modelled.
- **Chapter 5** investigates the steady-state operation by mean of a simulation model. The chapter is devoted to FEM model and optimization.
- **Chapter 6** sums up all the obtained results with a comment and future prospective

2 EXPERIMENTAL METHODS

The aim of this chapter is the description of the techniques used for the fabrication and characterization of the µ-reformer. The fabrication process of the micro-reformer is described in chapter 3.

2.1 MICROFABRICATION

Microfabrication refers to the process of fabricating small structures on a micron or smaller scale. Currently, it is a well-known manufacturing process that was created within the microelectronics industry. Miniaturization of devices presents challenges in many areas of science and engineering: physics, chemistry, materials science, computer science, ultra-precision engineering, fabrication processes, and equipment design. To fabricate a micro device many processes have to be performed and also repeated, typically it starts with the deposition of a thin film that is removed following the desired path. Generally, these devices are supported by a substrate due to the small dimension. The substrate also plays a structural role and allows an easy handling of the device. The kind of material used depends on the application, for example in electronic applications silicon wafers are generally used. All the processes are made in cleanrooms, where the air is humidity, temperature and particles contamination are well controlled. The dimension of dust, bacteria or smoke is in the order of micro-meter so they would affect the functionality of the final device.

2.1.1 Thin film deposition

The techniques used for ceramic thin films deposition can be divided in two main categories: Physical Vapour Deposition (PVD) and Chemical Vapour Deposition (CVD). In physical depositions only thermodynamic, mechanical or electromechanical processes are involved. Examples of PVD are: thermal evaporation, sputtering, Pulse Laser Deposition (PLD). On the contrary, in chemical depositions chemical processes are also involved. Generally, a fluid precursor reacts on the solid surface leaving a layer. Examples of CVD are: Chemical Bath Deposition (CBD), Atomic Layer Deposition (ALD), spin coating. However, both processes are highly affected by the deposition parameters (i.e. pressure, temperature, concentration).

2.1.2 Photolithography

Photolithography is a common process used in microfabrication used to transfer a pattern to substrate. The procedure is based on sequential steps. First, the wafer is chemically cleaned in order to remove any kind of impurities. Then a layer of photoresist resin is applied to the surface and, generally, is homogenized by spin-coating, a high-speed centrifugal whirling. After that, a mask containing the desired path is accurately aligned on the upper wafer surface and the photoresist is exposed to a high intensity ultraviolet light. Depending on the type of photoresist, negative or positive, it will behaves differently. If negative, the exposure to UV light polymerize the resin make it difficult to be removed.

If positive it behave the opposite, after the exposure the resin became soluble and will be removed by the developer. In fact, after the exposure a solvent (developer) will dissolve the resin according to the type (positive or negative).

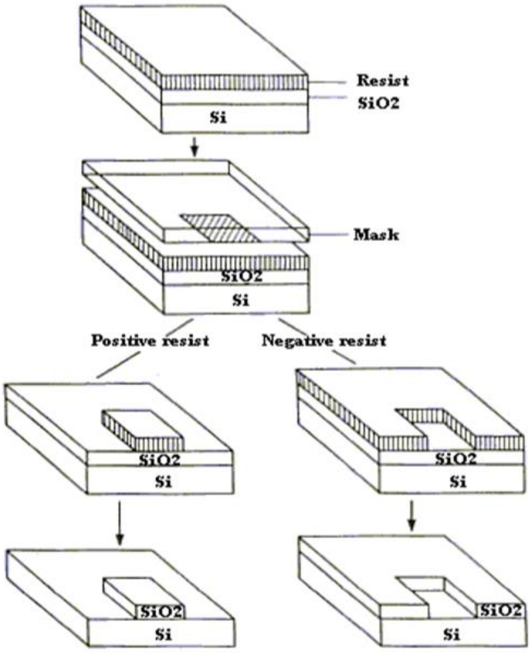

Figure 8- Schematic procedure of photolithography (https://static1.squarespace.com)

2.1.3 Etching

Etching is an intaglio method of printmaking. After the pattern is defined by the photolithography, it is transferred to the substrate by chemical or physical removal. There are two types of etching: wet etching and dry etching. Wet etching is realized with liquid-phase etchants. The wafer is immersed in a bath of etchant in order to remove the desired material. Dry etching is performed a chemically reactive plasma. The ions are accelerated by an electric field and, hitting the sample, they etch the material. The gas and the striked out material are exhausted by vacuum pumps. There are two other kind of dry etching: RIE and DRIE. RIE (Reactive Ion Etching) is a synergistic process between chemically active species and energetic ion bombardment, is an anisotropic process with reduced lateral etch. DRIE (Deep Reactive Ion Etching) has the same principle of RIE, but allow a deeper high-rate etching.

2.2 CALIBRATION OF SUSPENDED μ-REFORMER BY RAMAN SPECTROSCOPY

2.2.1 Raman spectroscopy

Raman Spectroscopy is a non-destructive technique which provides detailed information about chemical structure, phase, crystallinity and molecular interactions. This is a spectroscopy used to determine the vibrational and rotational modes of the molecules and it is based on inelastic scattering of photons (Raman Scattering).

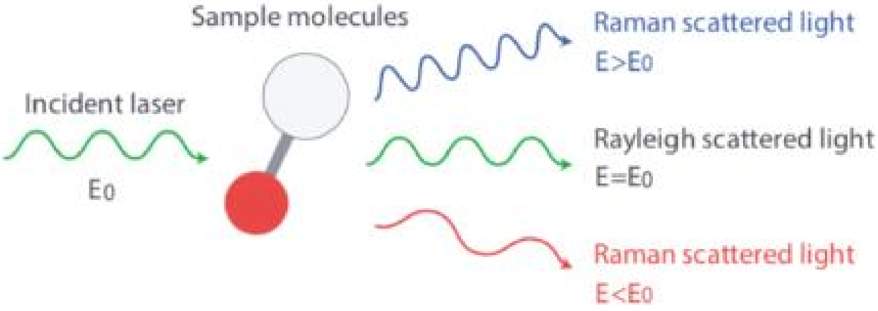

Figure 9- Scattering of light (https://www.nanophoton.net)

The source is usually a monochromatic light in the visible range, also X-rays can be used. The light beam, generally generated by a laser source, interacts with the vibration of the molecules and phonon of the sample to be characterize, producing an energy change in the laser photons. A schematic of the Raman working principle is presented Figure 10.

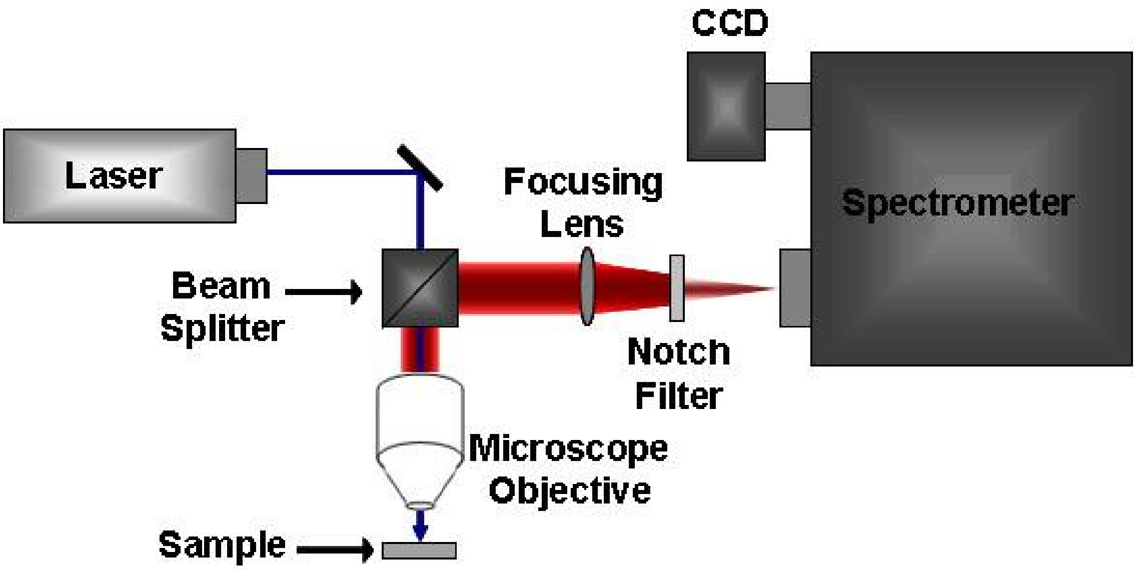

Figure 10- Working principle (http://cnx.org/)

The Raman scattered radiations are collected by a lens and directed to a monochromator. Instead, the elastic scattered radiations are filtered out, they have the same wavelength of the incident beam so they don't give any additional information. Only about 0.001% of the incident light produces inelastic scattering, so it is very difficult to separate it from the intense signal of the elastic scattering.

Raman spectral libraries are often used for identification of a material based on its Raman spectrum, libraries containing thousands of spectra are rapidly searched to find a match with the obtained spectrum.

2.2.2 In-situ Raman spectroscopy

In-situ Raman spectroscopy is a technique that allow to perform Raman spectroscopy directly under operating conditions. For instance, it can be possible to use a linkam in order to perform the measurement in certain condition (i.e. high temperature, vacuum condition). The linkam is made of 2 main component the stage and the temperature controller. The stage is made of a chamber in which is located a heating plate that, also, is where the sample is placed on. The chamber is closed by an hermetic lid for maintaining the desired conditions. It is also possible to inject a fluid flow or create vacuum condition by connecting a vacuum pump. Furthermore, electrical connections can be realize within chamber. The controller allow to manage the temperature inside the chamber.

Figure 11-Linkam stage and controller (www.linkam.co.uk)

In this work, in-situ Raman was performed to calibrate the temperature of the micro-reformer under operation. The calibration was performed with the help of a linkam stage. The set-up is shown in section 4.2. The measurement was performed in vacuum condition and it was imposed a power by applying an external current and voltage to the sample. The power of the laser was set to 100 mW with a wavelength of 545 nm (green light). It was used a long distance 50x objective.

2.3 CATALYST DEPOSITION AND CHARACTERIZATION

2.3.1 Atomic Layer Deposition (ALD)

Atomic Layer Deposition is a technique used for thin films deposition onto a substrate. It also is a layer-by-layer deposition that provides an optimal surface control and can produce thin, uniform and pinhole-free films over large areas. The process involves the surface of a substrate interacting with different precursors (reactants) in a cyclic mechanism. In each pulse an atomic layer is deposited, so the thickness will be directly proportional with the number of cycle.

It is a kind of Chemical Vapour Deposition (CVD), but with the peculiarity that the precursors are never present both in the same moment in the reactor, there is a precise sequence. The precursors react in a self-limiting reaction, this ensure that the reaction stops when all the reactive site of the substrate have been used. In Figure 12 is present a schematic of the process.

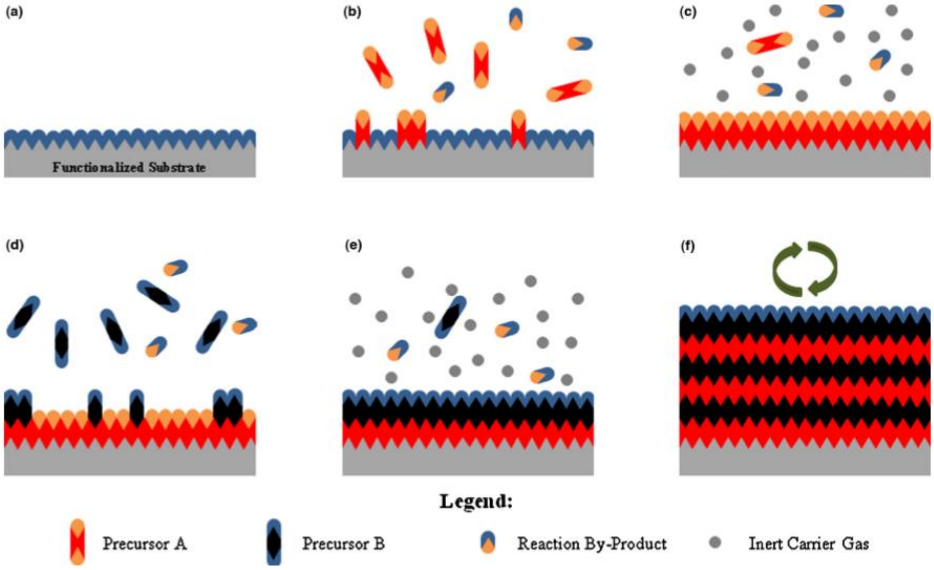

Figure 12- ALD deposition [19]

In Figure 12a the substrate is in the reactor and ready for the process. A pulse of the precursor A is sent (Figure 12b). The reaction by-products and the precursor in excess are purged with an inert carrier gas (Figure 12c). The same process is applied to precursor B, usually an oxidant (Figure 12d-e). The steps b-e are repeated till the final thickness is obtained (Figure 12f) [19].

In this work, ALD was used for the deposition of the catalysts in the channels of the µ-reformer. The catalyst was made by a γ-phase alumina support with a dispersion of nano-particles of platinum. The deposition of the alumina was carried out at 300°C in a vacuum chamber. The precursor used was TMA (trimethyl aluminium (III)) and the oxidant was H_20. Each pulse was characterized by 0.1 seconds flow of precursor follow by 6 seconds of purge. The number of cycles was 1200 accounting for a deposited thickness of around 100 nm. The deposition of platinum was also carried out at 300°C in vacuum condition. The precursor used was methylcyclopentadienyl platinum (IV) and the oxidant was O_2. The number of cycle was 120 aiming to create a dispersion of nano-particles of platinum.

2.3.2 Rapid Thermal Processing (RTP)

Rapid Thermal Processing is referred to the processes that involve high temperature and small timescale. This process is typically used in semiconductor manufacturing for activate the dopant or change the phase of the materials. The sample is rapidly heated from room temperature to high temperature (even more than 1000°C), then the cooling is controlled and the temperature is brought down slowly to avoid the breaking of the sample due to thermal shock. The rapid heat-up of the sample is usually performed with high intensity lamp or laser.

In this work, a RTP thermal treatment was performed after the ALD in order to crystallize the amorphous structure of the as-deposited alumina. The sample was heated-up by a lamp with a temperature ramp of 15°C/sec up to 850°C and kept to this temperature for 3 minutes.

2.3.3 Ellipsometry

Ellipsometry is a non-destructive thin film characterization technique. The working principle is based on the change of the polarization state of light reflected by a thin film. It can be used to determine composition, thickness, optical absorption and other material properties.

A light is emitted from a light source, polarized by a polarizer and directed to the sample. A linear polarization is performed when the components of the p-plane and the s-plane are in phase. After the reflection the two component of the electric field will be changed and modify the polarization in elliptical. Then a modulator and an analyser will restore the linear polarization. In order to generate a measure, is present a monochromator before the detector that separate the different light wavelength [20]. The working principle is shown in Figure 13.

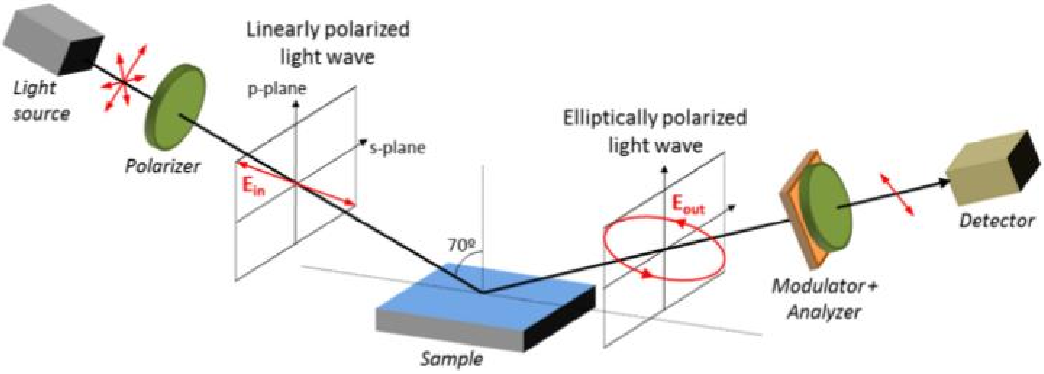

Figure 13- Ellipsometry working principle [20]

In this work, ellipsometry was used to estimate the thickness of the deposited catalyst on the sample. The range of the light source was 0.6-5 eV and the measured thickness was 100 nm.

2.3.4 Scanning Electron Microscope (SEM)

Scanning Electron Microscope is a type of electronic microscope that doesn't uses the light as source of radiation, but the beam is generated by an electronic source. Electrons are used because of they have a much smaller wavelength than light, allowing better resolution images. Typically a tungsten filament produces a beam of primary electrons that, after passing through a series of lenses to produce a focused beam, hit the surface of the sample. The sample is inside an evacuated chamber and, due to the interaction with the primary electron beam, generating various signal. Usually are detected secondary electrons and backscattered electrons. The secondary electrons, result of inelastic interactions between electron beam and sample, provides information about the surface and microstructure. The backscattered electrons, result of elastic electron-sample interaction, come from deeper regions of the sample and can provide information about the chemical composition of the material. In Figure 14 is shown a schematic of the basic components.

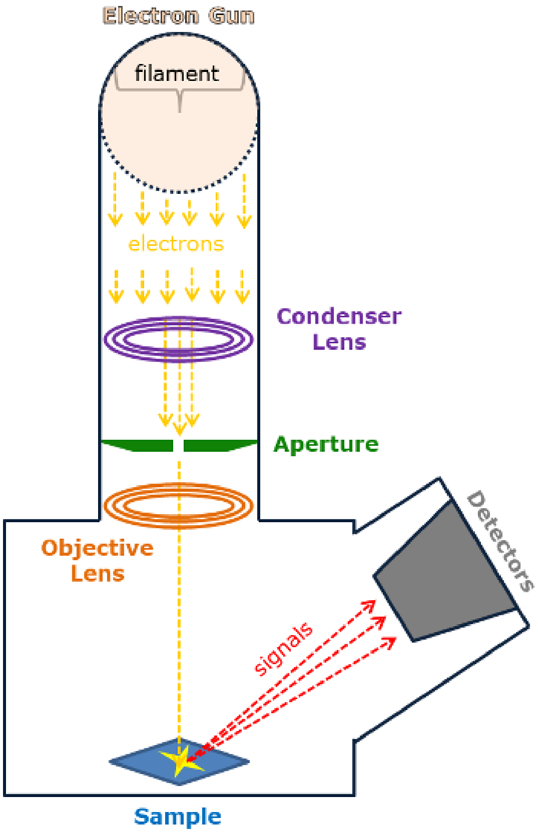

Figure 14- Schematic of basic SEM components (https://study.com)

In this work, SEM was used to study the cross section of the sample. Cross section was used for evaluate the deposition of the catalyst by ALD. Moreover, it was used also to check the condition of the µ-heater.

2.3.5 Energy dispersive X-Ray Spectroscopy (EDX)

Energy-dispersive X-ray spectroscopy is an analytical technique working with X-rays generated by an electronic beam hitting the sample. By analysing the emission spectrum is it possible to characterize a specific element since the energy of the emitted photons is characteristic of one specific electronic transition. It is also possible to quantify the atomic composition of the sample if the equipment is calibrated. The working principle is basically the same of the SEM, but with the detection of X-rays.

In this work, EDX was performed for characterizing the catalyst after the ALD deposition.

2.4 ANALYSIS OF REFORMED FLOW

2.4.1 Micro-gas chromatography (µ-GC)

The micro-gas chromatography is an analytical technique that separates and analyses the compounds of a gas mixture. Firstly, the mixture is injected inside the micro-gas chromatographer and enter in some metals tubing called columns. In each column there is a carrier gas passing inside, usually an inert gas (i.e. Argon, Helium), and a microscopic layer of liquid on the wall. The gaseous compounds, carried by the inert gas, interact with the walls and are eluted a different time, known as retention time. By the comparison among the retention time is possible to distinguish the various compounds of the mixture. Moreover, if the device is calibrated is possible to perform a quantification analysis.

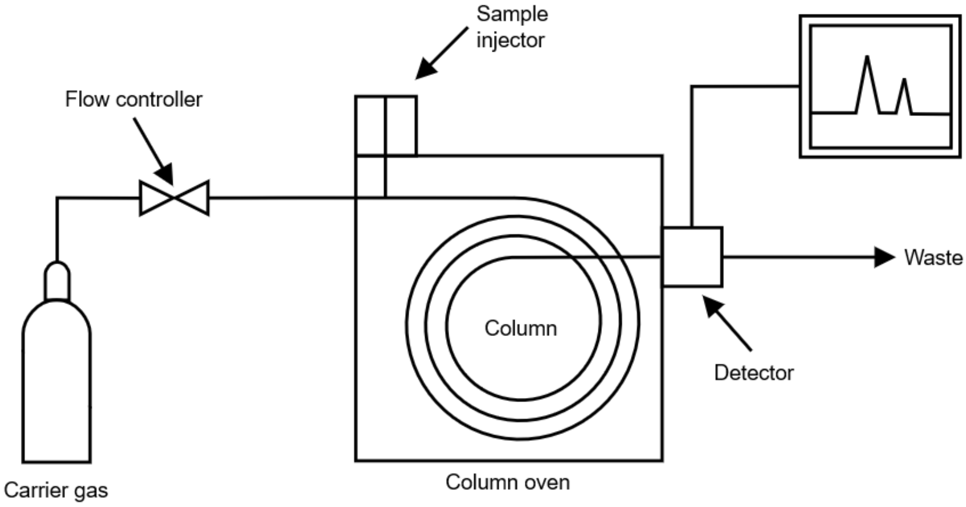

Figure 15- micro-GC schematic (Wikipedia)

In this work, the µ-GC was used for characterize the reformed flow. The equipment was characterized by 2 columns with 2 different carrier gas. One column was using Helium and the other one Argon. The hydrogen was detected in the column with Argon as carrier gas due to the difference in atomic number. Since helium and hydrogen have almost the same atomic number, detecting hydrogen in the column with helium as carrier gas was more complex.

2.5 FINITE ELEMENT METHOD (FEM)

The description of the physicals phenomena is generally expressed by a set of partial differential equations (PDEs). However, it is not possible to solve these PDEs by analytical methods for majority of problems and an approximation of the equations, generally based on discretization, can be performed. The PDEs are approximated with numerical model equations solved by numerical methods. The Finite Element Method (FEM) is one of the most used method to compute these approximation [21]. In order to solve the problem, the whole domain is divided into smaller parts called finite elements. The division is realized by the construction of a mesh of the consider geometry, the mesh represents the numerical domain for the solution. In this way, the domain that was continuum (infinite number of nodes) passes to a finite number of nodes allowing the resolution. Basically the domain in divided in a certain number of subdomains, each subdomain is represented by a set of equations and all the sets of equations are combined in a global system for compute final solution. The main supposition of this method is that each variable can be described as linear combination of basis functions. For example, a generic dependent variable v can be written as:

$$v \cong v_h = \sum_i v_i * \psi_i$$

Where v_i represent the coefficient of the function that approximate v with v_h, and ψ_i is the basis function that, for example, could have a value of 1 at ith node and 0 at other nodes.

For solving the PDEs with FEM, weak formulation has to be used. Weak formulation is an integral form that translate the equations from an infinite dimensional form into a finite dimensional space. Weak forms cannot compute perfectly accurate results because of the reduction in the requirements of smoothness, but still can compute very accurate solutions according to the mesh refinement.

In this work, FEM was used to model the thermal optimization of the sample in section 4.3.3 and the steam reforming reaction of DME in section 5.2. The used software was COMSOL Multiphysics.

3 MICROFABRICATION OF µ-REFORMER

This chapter describes the design, fabrication and functionalization of the device. The fabrication process is not part of the thesis because the sample was already manufactured before the beginning of the experimental part, even because it requires long time. However, a brief explanation of the fabrication steps is reported. Then the functionalization of the device is part of the work.

3.1 SUSPENDED µ-REFORMER

3.1.1 Design

The suspended µ-reformer is based on a 10x10 mm^2 Silicon chip with a thickness of 500 µm. The active area is the central 6x6 mm^2 square, composed by more than 7000 channels characterized by a diameter of 50 µm.. The innovation of this device is that the central active area is isolated by the external frame with a 50 µm air trench and it also has an own heating system. The two parts are linked together by a layer of 300 nm thickness of Si_3N_4. Silicon Nitride is the connection between the two parts and, since Si_3N_4 thermal conductivity is small (around 30 W/(m*K) at room temperature), the heat transferred by conduction is limited. The design is shown in Figure 16.

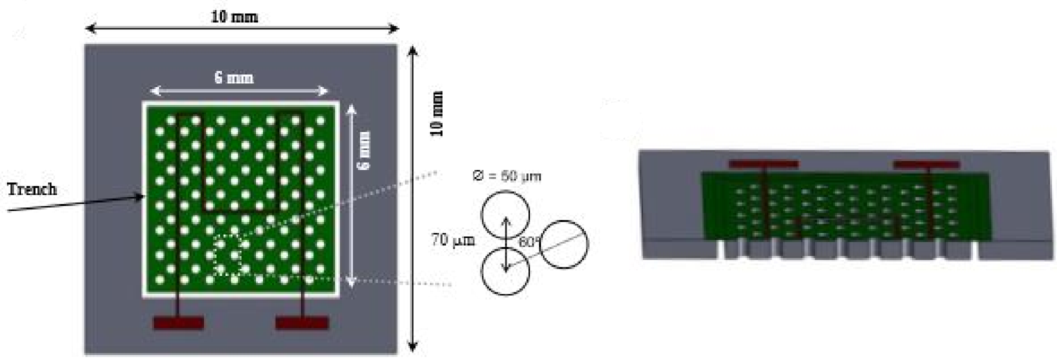

Figure 16- Suspended u-reformer [18]

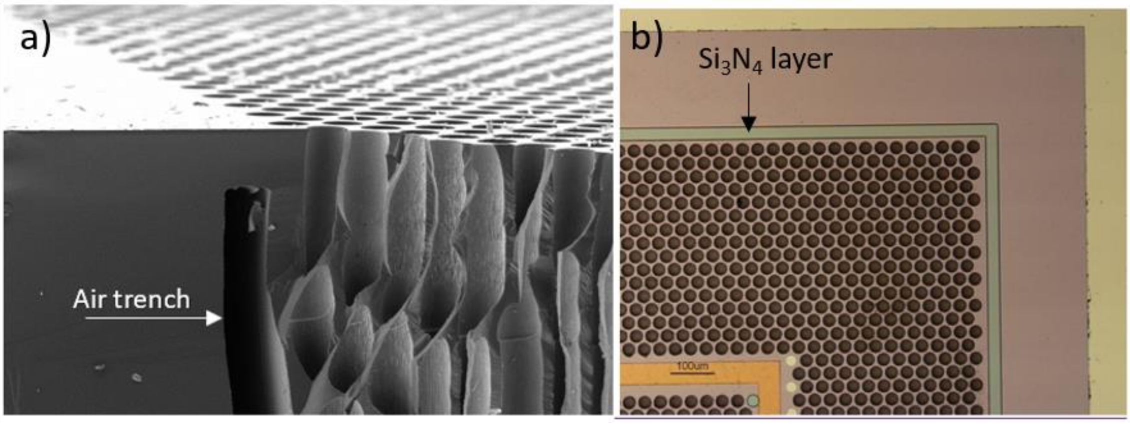

Figure 17- a) SEM image of cross section of the suspended u-reformer b) microscope image of the suspended u-reformer

Regarding the heating system, it is composed by a wire path of 3 different layer. The first layer, in contact with the surface, is a thin layer of titanium (30 nm) in order to create a good adhesion with the surface. The second, in the middle of the wire, is Tungsten (250 nm) that is the main heating layer and also the thickest one. The last one, in contact with the external ambient, is gold (50 nm) in order to protect the Tungsten from the oxidation. A cross section scheme of the wire is shown in Figure 18. The ends of the wire are two pads where is possible to impose, by connecting an external source, a current thus generate heat by Joule effect along the wire according to the relation:

$$P = R * I^2 \quad (W)$$

Where *R* is the overall resistance of the wire and *I* is the imposed current.

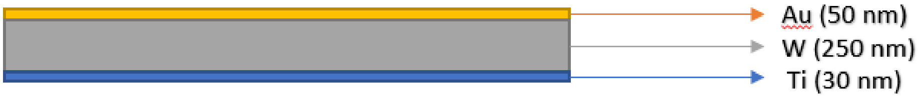

Figure 18- Schematic cross section of heater

3.1.2 Microfabrication steps

The microfabrication steps followed to obtain the final device are reported in Figure 19. P-type single crystal (100)-oriented silicon wafers with a thickness of 500 µm were thermally oxidized at 1100 °C to obtain a layer of 100 nm of SiO_2 (Figure 19A-B). Then with a Low-Pressure Chemical Vapour Deposition (LPCVD) was deposited a 300 nm thick layers on both sides (Figure 19C). In this way the wafers were passivated. On the front side of the wafers a metallic multilayer (the heater) was deposited by sputtering: 30 nm of Ti, 250 nm of W, 50 nm of Au (Figure 19D). A photolithography was performed to shape the heater and the pads, the exposed areas were removed by wet etching (Figure 19E). After, the area was passivated with a Plasma-Enhanced Chemical Vapour Deposition (PECVD) layer 1 µm thick of SiO_2 (Figure 19F). A second photolithographic step was used to define the channels and the frame, the dielectric layer was removed by Reactive-Ion Etching (RIE) (Figure 19G). Then, another photolithographic step on the back side defined the channels, the frame and the air trench. The dielectric layer was removed always by RIE (Figure 19H). As final step, another photolithography step was performed to define the channels and the air trench on the back side, a hard mask 1 µm thick made of aluminium/copper was deposited by sputtering. A DRIE (Deep Reactive-Ion Etching) process was realized to form the holes and the trench, the top side was protected with 2 µm thick resin layer. Finally, the aluminium/copper mask was chemically removed (Figure 19H-I) [18].

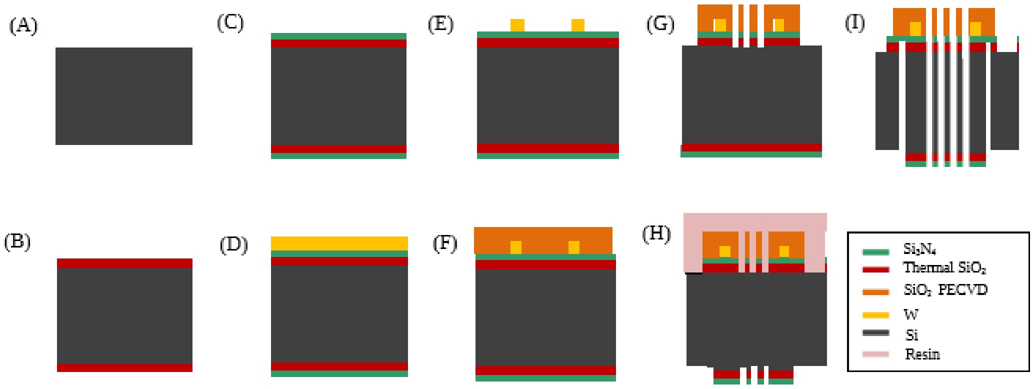

Figure 19- Fabrication steps of u-reformer [18]

3.1.3 Functionalization

The catalyst is a substance that helps a chemical reaction, but it is not consumed by it. Each chemical reaction is characterized by an activation energy, the energy that must be provides to the reactants for obtaining the products. The role of the catalyst is to reduces this energy barrier offering a different route for the reaction that requires less energy.

The steam reforming of DME, the fuel used in this work, is a relatively low temperature process (350-500°C) and requires the presence of a bifunctional catalyst, one acid component and one metallic component. The reaction was catalysed as follow:

DME hydrolysis on acid sites:

$$CH_3OCH_3 + H_2O = 2CH_3OH$$

Methanol steam reforming on metal sites:

$$CH_3OH + H_2O = 3H_2 + CO$$

There was also the production of methane, generated by the presence of the acid sites. When higher temperatures were reached, DME thermal decomposition took place as well [22]:

$$CH_3OCH_3 = CH_4 + H_2 + CO$$

Reaching higher temperature was also a problem because of the coke formation and deposition. The coke deposition is responsible of the catalyst deactivation because reduces the catalyst active area.

The same bifunctional Pt/Al_2O_3 catalyst was also adopted for the DME partial oxidation reaction [23]. In this case the main reaction to be catalysed was:

$$CH_3OCH_3 + \frac{1}{2}O_2 = 3H_2 + 2CO$$

In this work a catalyst layer was deposited by Atomic Layer Deposition (ALD) (properly explain in the section 2.3.1) in the walls of the channels. Alumina has been chosen as acid component and platinum as metallic component. First, a 100 nm thick homogenous layer of γ-phase alumina (γ-Al_2O_3) was deposited. Then, the metallic phase was deposited in form of nanoparticles dispersed on the first alumina layer.

It was analysed the cross section of the sample in order to verify the presence of the alumina inside the channel. Figure 20 shows a SEM image of the alumina pillars inside one of the several channels of the sample. The alumina layer was well deposited and appeared homogeneous on the walls of the channels. This was the catalytic support layer on which the nanoparticles of platinum were dispersed by ALD. The Pt particles are not visible in this image because they are too small or because the deposition didn't work perfectly.

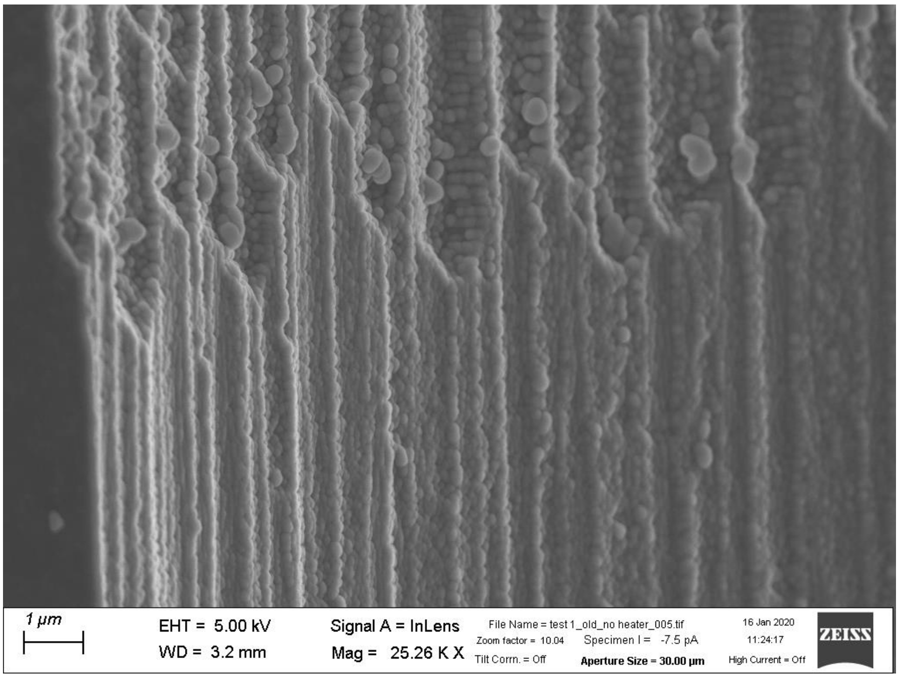

Figure 20- Alumina pillars. SEM image of the sample cross section

4 TESTING AND CALIBRATION OF SELF-HEATED μ-REFORMER FOR FAST START-UP

4.1 INTRODUCTION

The aim of this chapter is to calibrate and test the performance of the self-heated μ-reformer. The analysis was focused mainly on the heater of the μ-reformer for the evaluation of the start-up condition. The steady state conditions is analysed in chapter 5.

4.2 CALIBRATION OF THE HEATER

The first experimental step was the calibration of the heater of the μ-reformer. The aim was to find a calibration curve of the heater. A calibration curve is a curve that allow to measure a parameter indirectly, as a function of the output values of the experiment. In this case, was performed a Raman in-situ measurements of the sample's temperature as a function of the electrical power supplied. In this way, by following the shift of the main Si Raman mode, an estimation of the device temperature as function of the ohmic resistance of the heater was founded, also confirmed by a thermal FEM model (section 4.3.2).

4.2.1 Set-up

The experimental set-up is shown in Figure 21. The sample was located in the chamber inside the linkam stage. Between the sample and the hot plate of the stage there was a glass holder, where the sample was placed on. It was used a vacuum pump in order to create a vacuum of 0.812 mbar inside the chamber. Then, it was imposed an external power to the heater of the sample. Silver paste was used to implement a good electrical connection between the pads of the heater and the ends of the wires. The power supplied was manually managed from the external power source. The laser beam, after interacting with the sample, was collected from the detector and directed to a monochromator (not represented in the figure).

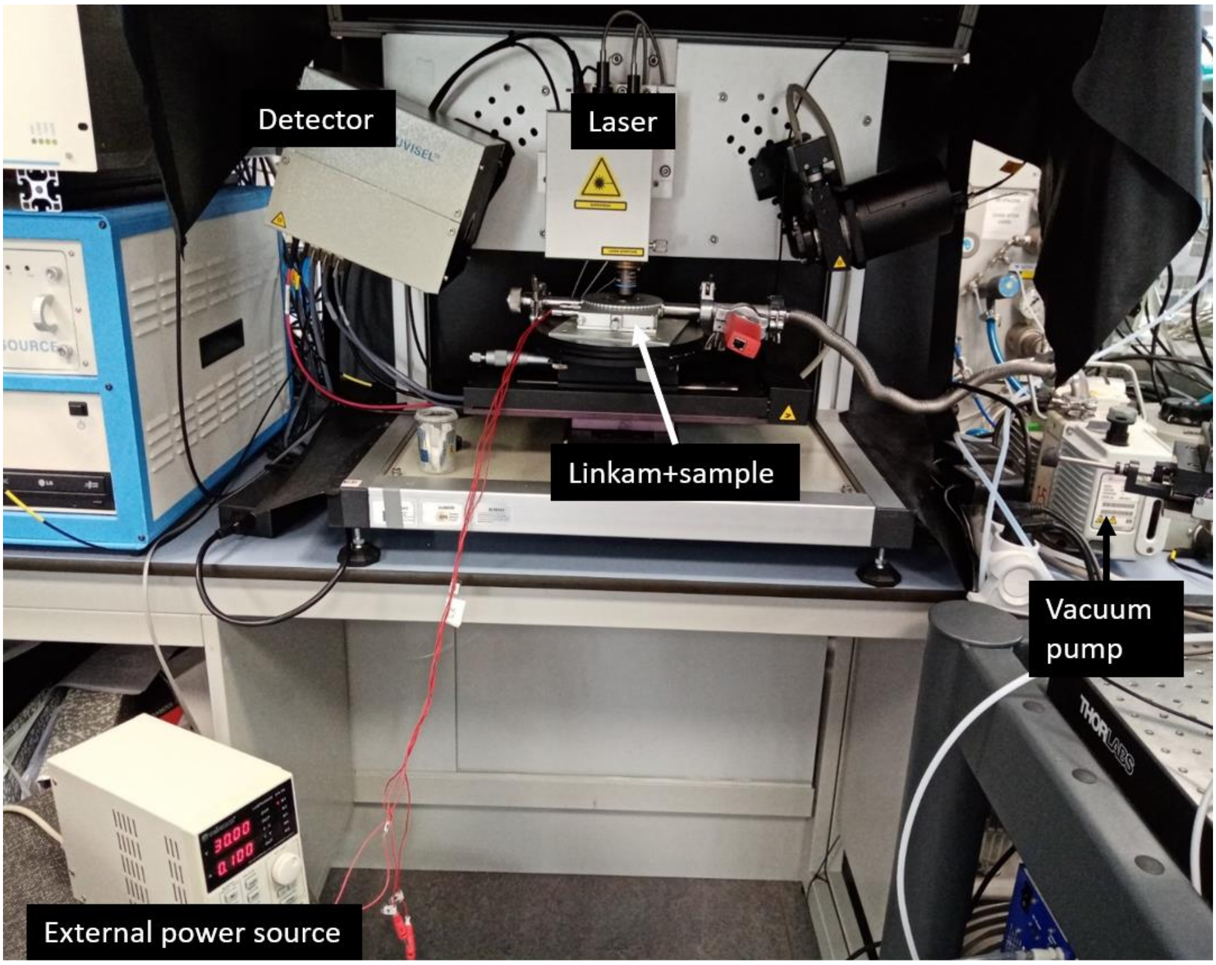

Figure 21-Experimental set-up for in-situ Raman

4.2.2 Results

The Raman spectroscopy provides information on the structure of molecular vibrational energy levels. In this particular case, this information was exploited for the evaluation of the temperature. As the temperature increases, the bond length increases and, as consequence, the energy of the vibrational mode decrease. Vice versa, a temperature decrease lead to a shorter bond length and an increase in the energy of the vibrational mode. The increase or decrease in bond length causes a change in the vibrational force constant, which results in a shift of the Raman peak position [24].

Firstly, was calibrated the laser in the Silicon Raman shift at room temperature (521 cm^{-1}). Then, the measurement was performed by varying the input power from the external power source. The result is shown in Figure 22. In the x-axis was reported the energy in cm^{-1}, Raman shifts are typically reported in wavenumbers, which have units of inverse length, as this value is directly related to energy. 1 cm^{-1} is equal to 0.000123 eV [25], this unit is used to represent the inversely dependence from the energy by the wavelength ($E=h\nu=hc/\lambda$). The signal intensity is represented in the y-axis in arbitrary units. It is important to notice that the peaks between two different temperatures were shifting in few seconds. Thus, the thermal inertia of the sample was very low and this is one of the most important behaviour to ensure a fast start-up of the device.

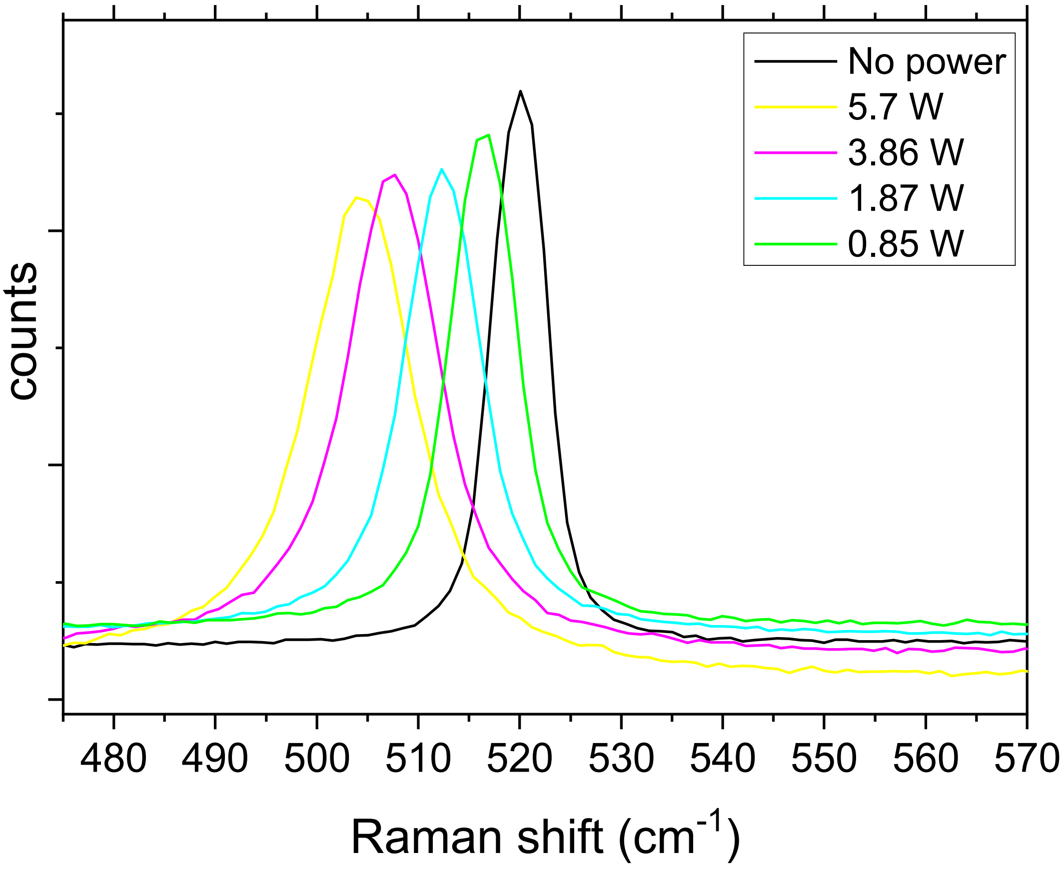

Figure 22- Raman shift for different input power

The measurement was performed in the range of power between 0-5.7W, that was the maximum limit of the power source. In order to convert this information into temperature values, it was used as reference the calibration made in a previous study [26] . The used curve for the evaluation is shown in Figure 23. For the conversion was used and reported only the graph (a) of the original figure. The Raman Shift corresponding to room temperature was 521 cm^{-1}. The slope of the curve was -0.022 and the conversion was computed as follow:

$$T = \frac{Peak_{reference} - Peak_{measured}}{slope} + T_{reference}$$

Where $Peak_{reference}$ is 521 cm^{-1}, $Peak_{measured}$ is the measured Raman shift peak in the experimental condition and $T_{reference}$ is the temperature of the reference peak (25°C).

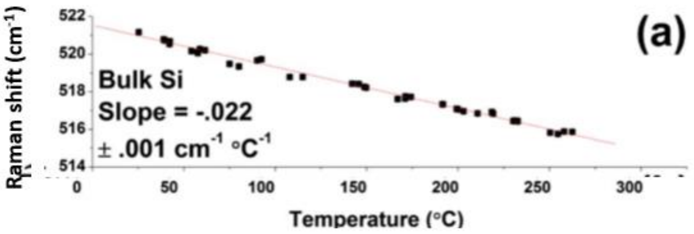

Figure 23- Reference for the conversion in temperature of the Raman Shift [26]

By the conversion of the Raman shift peaks in temperatures, it was obtained an evaluation of the resistance in function of the temperature. The resistance was known by the current and voltage input of the external power source. Since it was direct current, the resistance was calculated by the Ohm's law:

$$R = \frac{V}{I} \qquad (\Omega)$$

The voltage was varying in the range 8-30 V and the current was varying in the range 0.05-0.2 A. However, the external source was limited to a maximum voltage of 30 V.

The obtained trends are reported in Figure 24. First, the sample was heated up applying the maximum power of the external source, in fact the values number 1 and 2 presented a little deviation from the general trend probably due to the limitation of the voltage. Then, by reducing the applied power, the trend of the resistance (Figure 24-a) was linear and the trend of the temperature in function of the power was following a power law (Figure 24-b) as expected. However, it was reached a temperature higher than 700°C heating the sample only with the heater of the μ-reformer, this is the most important result shown in this graph.

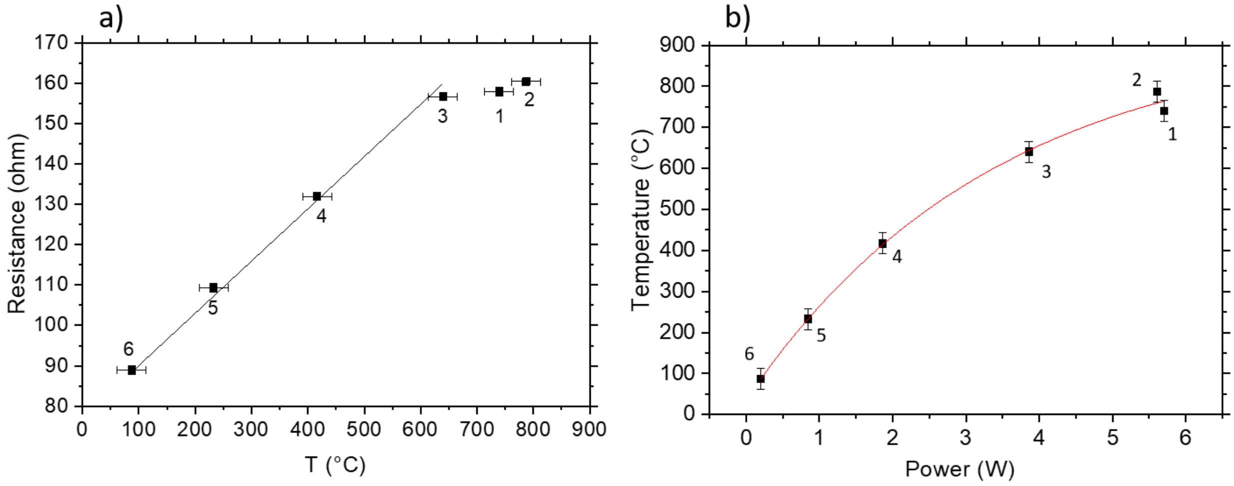

Figure 24- Calibration curves of the heater

The highest measured value was:

Raman shift (cm^{-1})	504.23
Voltage (V)	30
Current (A)	0.187
Temperature (°C)	787

In Figure 25 a detail of the sample during the calibration process is reported. As visible, the central part of the µ-reformer was turned in red. The red colour corresponds to a temperature of about 700 °C (about 970 K) as shown in the colour legend. Thus, this was the proof that the heater was heating the sample properly. In this case the applied current was 0.2 A and the applied voltage was 30 V.

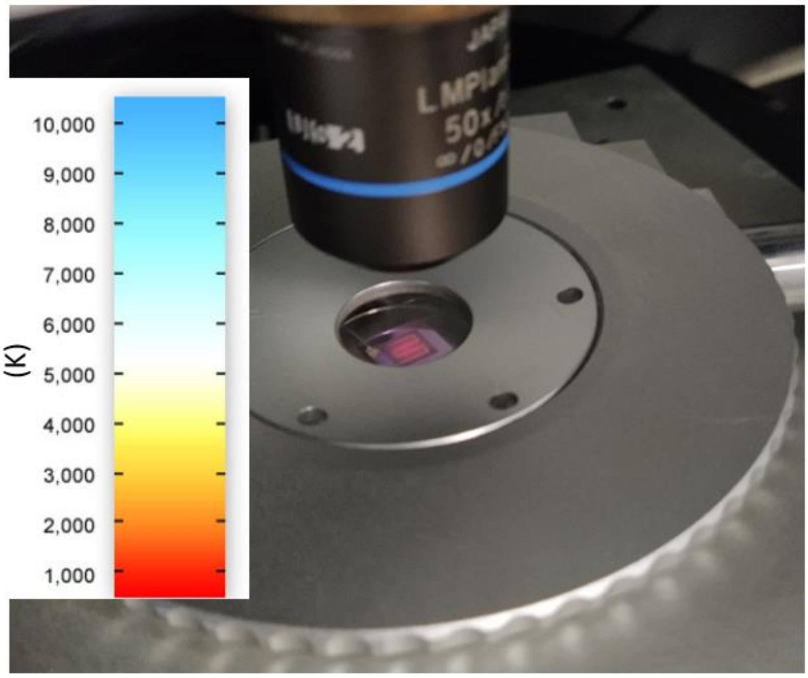

Figure 25- Detail while the calibration was carried out

4.3 THERMAL EVALUATION

4.3.1 Experimental results

Using the same experimental set-up for perform the calibration of the heater, it was also performed a map of the temperature of the sample. There were considered three relevant spot: the centre of the active area, the frame and the base of the sample. The temperature of the active area and the temperature of the frame were measured by in-situ Raman spectroscopy, exactly as the previous calibration case. While the temperature of the base was measured using the hot plate thermometer of the linkam stage, which roughly represents the thermal losses through the sample's base. In this last case, between the sample and the thermometer there were a glass as support layer.

As shown in Table *1*, when the centre of the sample was at 787 °C, the frame was at 640 °C and the plate at 120 °C. The insulation provided by the Si_3N_4 was not good as expected. The problem may be related on the presence of a 50 µm layer of Si with the role of support of the suspended active area.

Table 1- *Map of the temperature*

	Centre	*Frame*	*Hot plate*
Raman shift (cm^{-1})	504.23	507.47	\
Voltage (V)	30	30	\
Current (A)	0.187	0.179	\
Temperature (°C)	787	640	120

4.3.2 Simulation model

4.3.2.1 Model parameters

In order to better understand the reason why the insulation was not working as expected, a FEM model was developed. It was performed only on a thermal simulation of the sample trying to reproduce the experimental conditions.

The geometry of the system was composed by the µ-reformer and the support glass layer, the domain and the mesh are shown in Figure 26. The distribution of the nodes was concentrated more in the point where a big difference of temperature was expected. In particular in the connection layer between the frame and the central area.

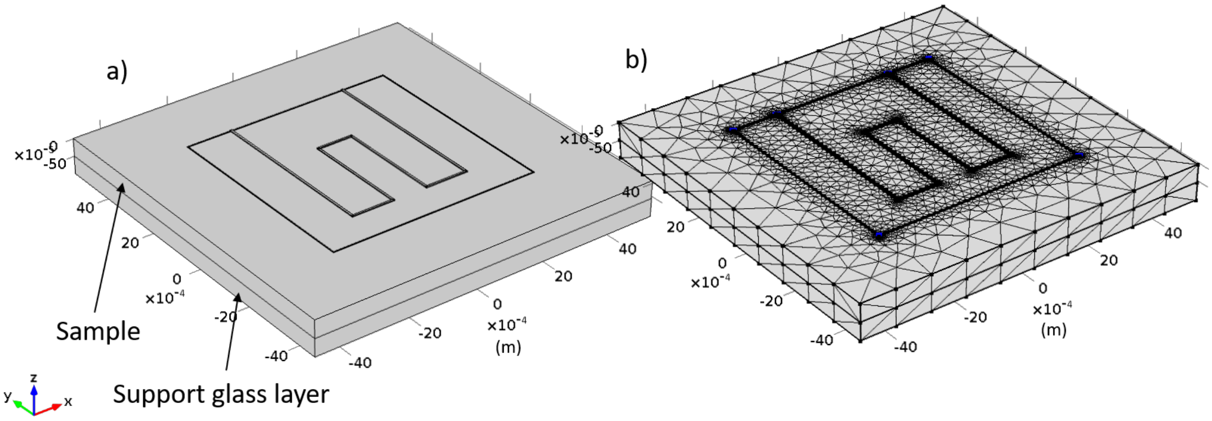

Figure 26- Domain (a) and mesh (b) of the thermal simulation

The *heat transfer* was the only physic considered in this simulation. The heat transfer mechanism taken in account were conduction and radiation. The convection was not included in the analysis because of the vacuum condition. The governing equation was:

$$\rho C_p \boldsymbol{u} \cdot \nabla \mathrm{T} = \nabla \cdot (k \nabla \mathrm{T}) + Q$$

Where ρ is the density, C_p the thermal capacity at constant pressure, k the thermal conductivity and Q the volumetric power generation.

The volumetric heat generation was imposed only on the serpentine-like heater of the sample:

$$Q = \frac{P_{tot}}{V}$$

Where P_{tot} is the power applied by the external source and *V* is the volume of the heater.

It was also considered the *surface-to-ambient radiation* for all the exposed surface of the domain except the surface that was touching the hot plate of the linkam stage, in which *thermal insulation* condition was applied:

$$-n \cdot (-k \nabla T) = \varepsilon \sigma \left(T_{amb}^4 - T^4 \right) \qquad\qquad -n \cdot (-k \nabla T) = 0$$

Where T_{amb} is the ambient temperature and was set equal to 25 °C, ε is the surface emissivity (for Si was equal to 0.7) and σ is the Stefan-Boltzman constant.

Finally, it was considered a *thin thermally resistive layer* for model the contact resistance between the two different materials (Silicon and glass), the heat flux across this layer was:

$$-n_d \cdot (-k_d \nabla T_d) = -\frac{T_u - T_d}{R_s} \qquad\qquad -n_u \cdot (-k_u \nabla T_u) = -\frac{T_d - T_u}{R_s}$$

Where the subscript “u” and “d” refers to the upside and downside layers and R_s is the thermal resistance. For modelling the experiment, it was chosen a values of the thermal resistance equal to 2 K*m^2/W. The temperature of the glass base was fixed to 110ºC, which was the temperature measured by the linkam substrate’s thermocouple.

In are resumed the conditions applied to the model:

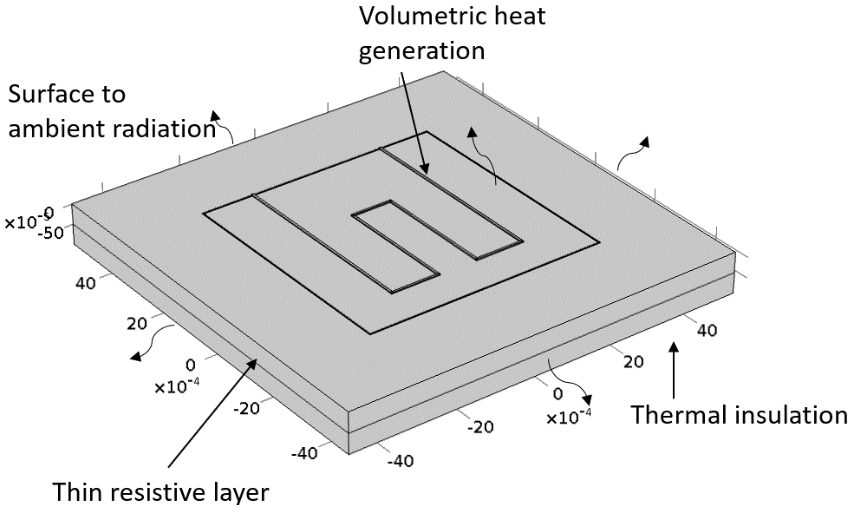

Figure 27- Thermal model conditions

4.3.2.2 Model results

The result of the simulation is shown in Figure 28. From the three different colours is easy to differentiate the three different spots. The highest temperature was reached in the central active area (red zone), then the frame is characterized by an intermediate temperature (yellow zone) and finally the glass support layer (blue zone) with the lowest value of temperature. The highest reached value of the temperature was 787 °C, but for evaluate the temperature of each zone it was calculated a surface average value. The average values of each zone are reported in Table *2*.

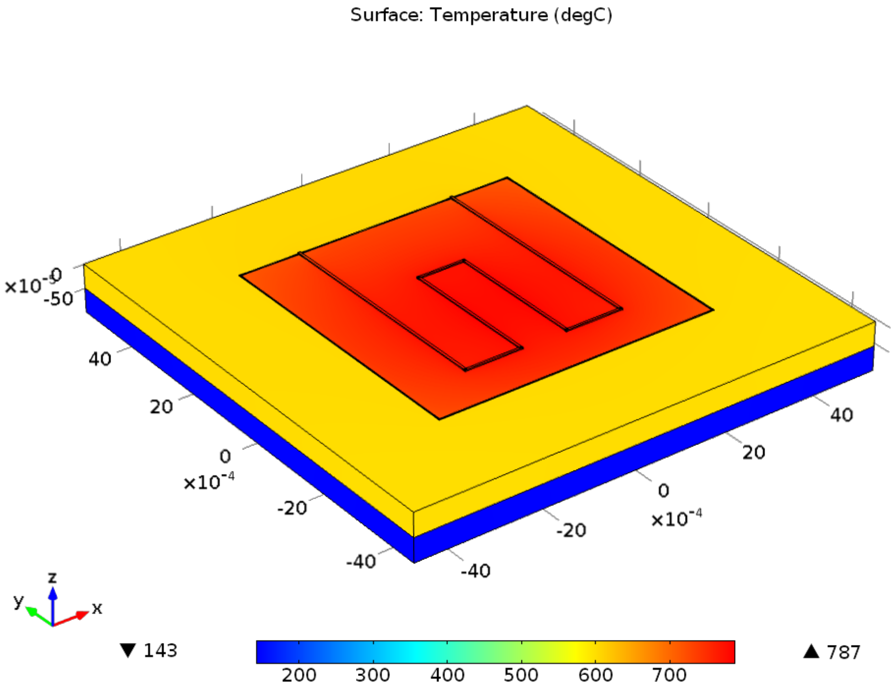

Figure 28- Temperature distribution with 5.5 W

For validate the model, the relative percentage error between the model and the experimental results was computed as follow:

$$err_{rel_{\%}} = \left| \frac{T_{model} - T_{experimental}}{T_{experimental}} \right| \cdot 100 \qquad (\%)$$

Table *2* reports the final results. As visible, the lowest relative error between the experimental measured temperature and the model result was obtained in the case of the centre temperatures of the device (3.43 %). Instead, the highest value of the relative error was obtained between the base temperatures (about 26 %). However, the average relative error was about 11 %.

Table 2- *Comparison between model and experimental results*

	Model results	*Experimental results*	*Relative error %*
Centre temperature (°C)	760	787	3.43
Frame temperature (°C)	603	640	5.78
Base temperature (°C)	145	115	26.08

4.3.3 Thermal optimization

After the model was validated, a thermal optimization was performed. The aim of the optimization was to obtain a better insulation between the central active area and the frame of the sample. In order to achieve this objective, it was removed the additional 50 µm thick Si layer from the domain. The result (Figure 29) was, as expected, a better insulation of the central active area. In fact, the Si additional layer was the main reason why the Si_3N_4 layer wasn't effective. The thermal conductivity of the Si is 148 W/(m*K) at room temperature [27], while the conductivity of the Si_3N_4 is 30 W/(m*K). Furthermore, the thickness of the Si layer was 50 µm compared to 5 µm of the Si_3N_4. Due to these motivations, the heat was dissipated through the Si layer, bypassing the insulator layer. Thus, removing the Si layer the insulation was performed only by the Si_3N_4 achieving a better result.

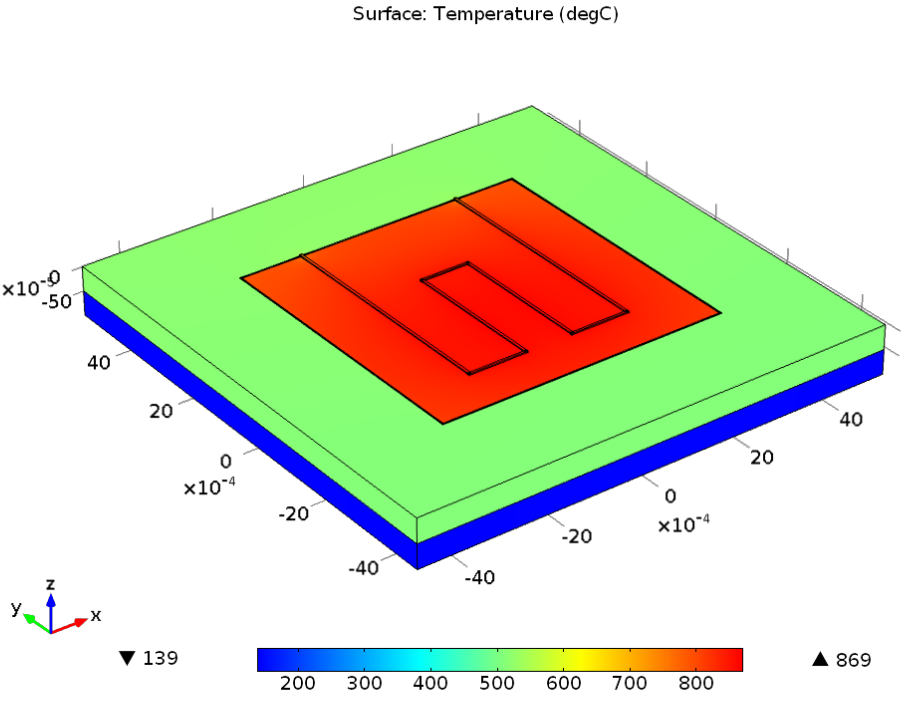

Figure 29-Temperature distribution with 5.5 W with only the 300 nm Si_3N_4 layer

The comparison was made considering a power supply of 5.5 W from the external source and between the average surface temperature of the 3 zones. The comparison (Table *3*) shows a huge difference between the 2 cases. In the original case the difference between the frame and the active area was around 150 °C, by removing the Si layer there was a big improvement in the insulation leading also to a substantial increase in the average temperature of the central zone. In fact, the average temperature varied from 760 °C to 850 °C. While the difference between the frame and the centre varied from 150 °C to about 360 °C. The temperature of the base was almost constant in the 2 cases because it was not affected by the thickness of the Si layer.

Table 3-*Comparison between original case and optimized case*

	With Si layer	*Without Si layer*
Centre temperature (°C)	760	850
Frame temperature (°C)	603	487
Base temperature (°C)	145	140

Finally, in Figure 30 is shown in detail the connection between the frame and the active area. Clearly, when the Silicon layer was present, there was not a big thermal gradient. The temperature of the two spot resulted more homogeneous with respect to the case in which the Silicon layer was removed. In fact, when there was only the Silicon nitride as connection, the layer was characterized by a big thermal gradient. This is the best configuration for the insulation of the central active area from the frame.

From the obtained measurements and simulations it can be deduced that etching the additional Si layer brings advantages for both insulation and power efficiency.

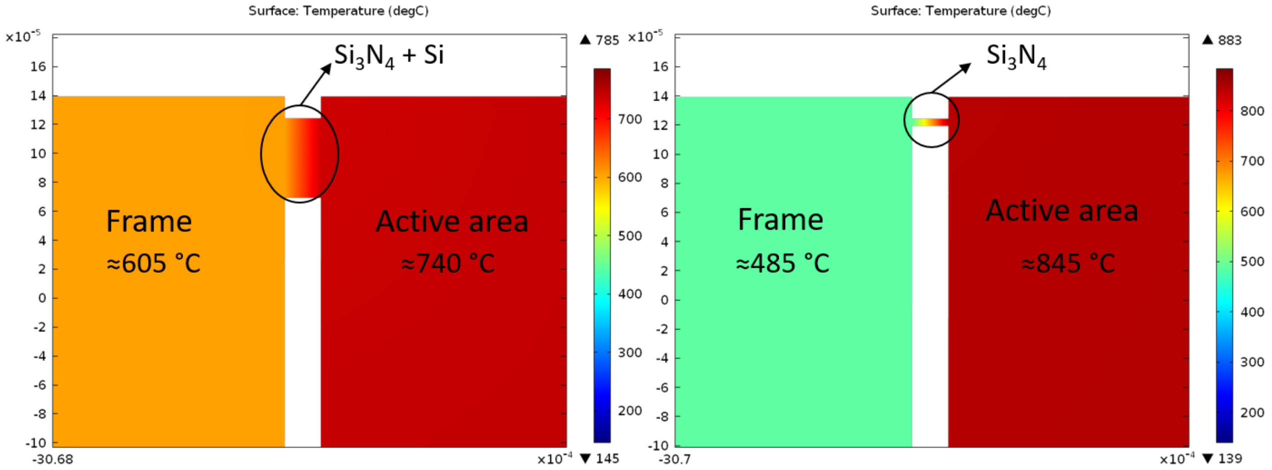

Figure 30- Heat dissipation comparison between the non-optimized and optimized configuration

4.4 CHEMICAL EVALUATION

4.4.1 Experimental set-up

After the thermal evaluation of the µ-reformer, an experiment was carried out in order to evaluate the efficency of the converison of the fuel.

Figure 31 shows the chosen set-up. Before running the experiment, a 20 ml/min flow of nitrogen and hydreogen was injected in the system in order to activate the catalyst and avoid the oxidation of the metl. The entering flow of liquid DME was controlled by a micro-mass flow controller. The DME was liquefied by pressure (about 7 bar), and after the flow rate controller, due to a drop of pressure and a heated tube, the DME evaporated in gaseos phase. The entering air flow was also regluated by a flow controller. After the regulation, the 2 flows were mixed and heated-up. The tube was heated-up to about 100 °C to ensure that DME was not condensing, but also for the need of a pre-heating of the flow before entering the reactor. Then, the heated mixture was entring the reactore where the DME was reformed. The reformed flow was sent firtsly to a condenser in order to condensate any possible liquid particles, and then was stored in a special bag. This step can be avoided, sending directly the reformed flow into the μ-GC. The last step was the analysis of the reformed flow performed with a μ-gas chromatographer.

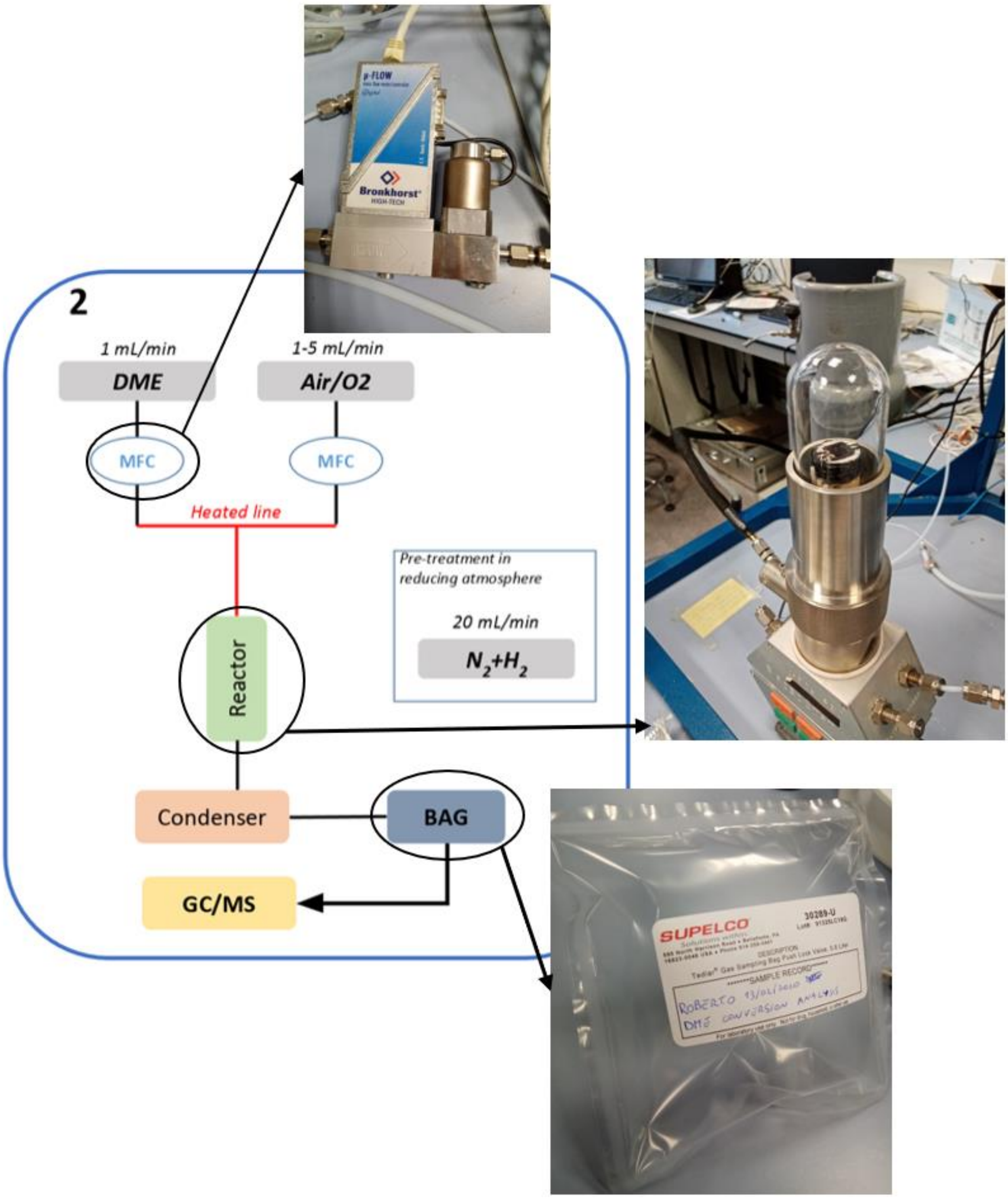

Figure 31- Experimental set-up

4.4.2 DME partial oxidation

The main reaction for the conversion of the DME are: DME steam reforming, DME partial oxidation. The reaction that was taking place inside the reactor was the DME partial oxidation. It is an exothermic reaction and, differently from the steam reforming reaction, there is no need of steam. The obtained products strongly depend on the catalyst used and on the working conditions. The main products over alumina supported catalyst are supposed to be CO, CH_4, HCHO, CO_2, H_2 and H_2O [28]. The partial oxidation is a relatively low temperature process and it could follow 2 different path: the thermal decomposition of the DME and the following oxidation of the decomposed species, or the direct oxidation by O_2:

DME decomposition:

$$CH_3OCH_3 = CH_4 + CO + CO_2$$

CO hydrogenation:

$$CO + 3H_2 = CH_4 + H_2O$$

Partial oxidation:

$$CH_3OCH_3 + \frac{1}{2}O_2 = CO + 3H_2$$

Complete oxidation:

$$CH_3OCH_3 + 3O_2 = 2CO + 3H_2O$$

Water gas shift:

$$H_2O + CO = H_2 + CO_2$$

In the temperature range below 350 °C, the partial oxidation is expected to be the most relevant reaction. Increase the temperature above 350 °C leads to an increase of CH_4 and CO_2 production [28]. However, the reactivity of the DME in partial oxidation condition is not deeply studied and is under development.

4.4.3 Results

The flow rates that were entering the system were: 1 ml/min of DME and 5 ml/min of air. It was applied to the heater of the reformer a voltage of 29 V and a current of 0.25 A accounting for a ohmic resistance of 116 Ω. According to the previous calibration of the reformer, the temperature of the sample was of around 370 °C.

The results of the micro-gas chromatography analysis showed a good percentage of hydrogen (around 12%). The percentages were calculated without considering the water, DME and N_2. The maximum detected was CO with a value of 62%, CO_2 was 26% and it wasn't detected any methane production.

The available equipment was not able to detected the DME, so it was not possible to quantify the conversion percentage.

Table 4-*Result of the μ-GC*

Specie	*Percentage (%)*
H_2	11.9
CH_4	0
CO	62.1
CO_2	26

The results were sufficiently good since the μ-heater was the only heat supplier. The conversion can be improved, because of two reasons. First, because there was a very low quantity of platinum deposited by ALD. The alumina layer was successfully deposited catalyst, but the metal component of the catalyst was not well attached. The other motivation is shown in Figure 32. In Figure 32-a is shown the new heater, without any deposition process. The other two images show the heater after the ALD deposition. The heater is visibly damaged by the process. Between the Figure 32-b and Figure 32-c there are no substantial differences, the damage of the heater is almost the same. The combination of this two motivations, could have caused the problem in the conversion. Thus, by improving the Pt deposition and by protecting the μ-heater, better results can be achieved. Another improvement could be to measure the operating temperature of the experiment.

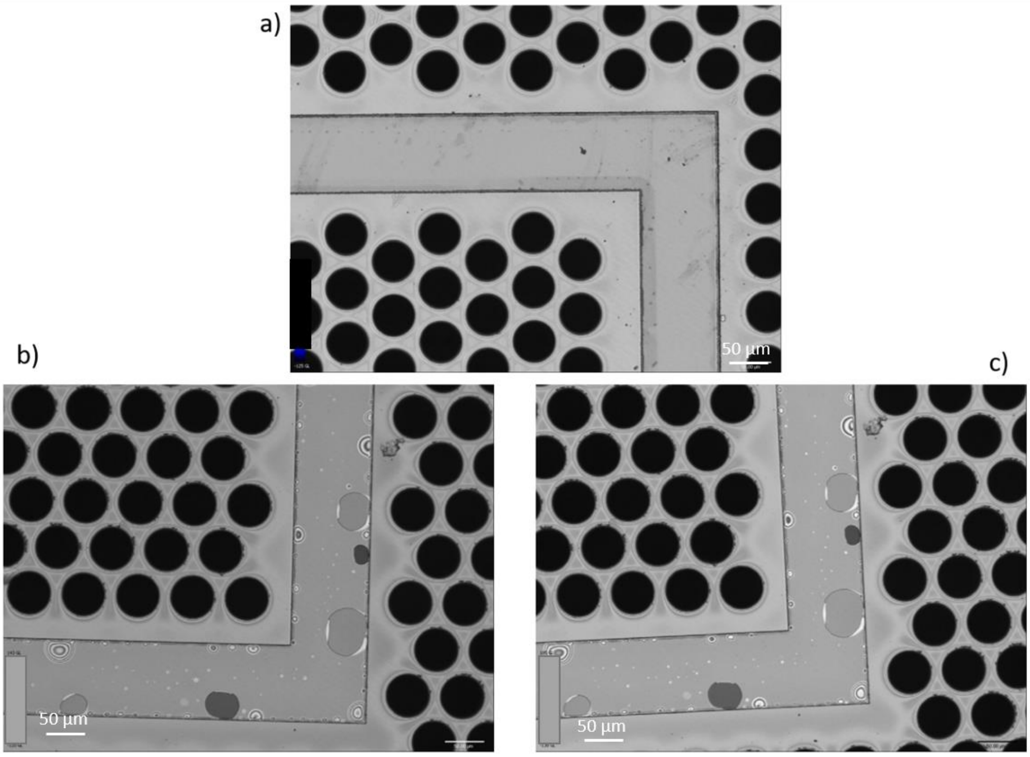

Figure 32- a) new sample b) heater after ALD depostion of alumina c) heater after ALD depositon of Pt

It is important to notice that the heater of the samples that were subjected to RTP treatment was very damaged. Figure 33 shows the confocal microscope image (a) and also the two SEM images(b-c). It is clear that the performance of the heater in these conditions was worse. Thus, the RTP treatment was no more performed in order to protect the functionality of the heater.

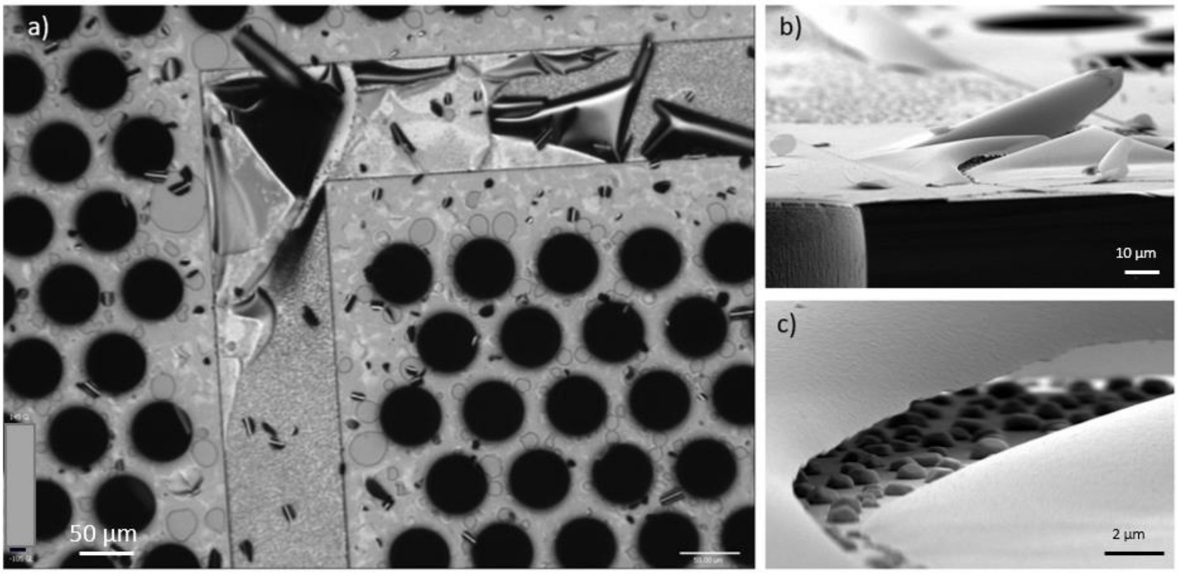

Figure 33-a) confocal microscope images of the heater after RTP b),c) SEM images of the heater after RTP

However, the results of the conversion were good and they can be also improved. Hydrogen was produced heating the system only with the µ-heater. There is also a good percentage of carbon monoxide that can be used as fuel for the µ-SOFC. Thanks to this experiment, it was proved that the µ-reformer can be implemented in the µ-SOFC PG system.

5 UNDERSTANDING THE PERFORMANCES OF STEADY-STATE μ-REFORMER

5.1 INTRODUCTION

The objective of this chapter is to estimate and optimize the performances of the device through a Finite Element Method simulation. The experimental data, which the simulation is model on, are taken from a previous experiment based on DME steam reforming reaction. The experiment was carried out in a steady-state condition in which the own heater of the μ-reformer was not used and the sample was heated in an oven, assuring a thermal homogeneity in the structure.

5.1.1 Description of set-up

The adopted set-up is shown in Figure 34. First of all, a 300°C flow of N_2 and H_2 was injected for one hour before starting the experiment in order to activate the catalysts and avoid the oxidation of the metal catalyst. After that, it were injected the reactants. The incoming Argon flow, used as carrier gas, was passing through a bubbler containing water for humidify the flow. The process was performed at 50°C in order to reach the desired percentage of steam (12%). The DME, liquified by pressure, entered the system in a liquid phase and was regulated by a mass flow controller. After the regulation, due to a drop of pressure and an increase of temperature, DME evaporated. The mix of gases was heated-up before entering the furnace for two reasons: ensure that water and DME were in gaseous form and avoid a huge temperature gradient when the flow entered the furnace. The red lines in the picture indicate the heated-up tubes. The μ-reformer was located inside the furnace in a proper sample holder and kept at constant temperature. After the reaction, the flow passed through a condenser in order to condense all the possible liquid particles and, consequently, a micro-gas chromatography was performed.

Was entering the system: 0.5 ml/min of DME; 24.6 ml/min of Argon, of which 12.2% was steam. Steam/carbon ratio was equal to 3.

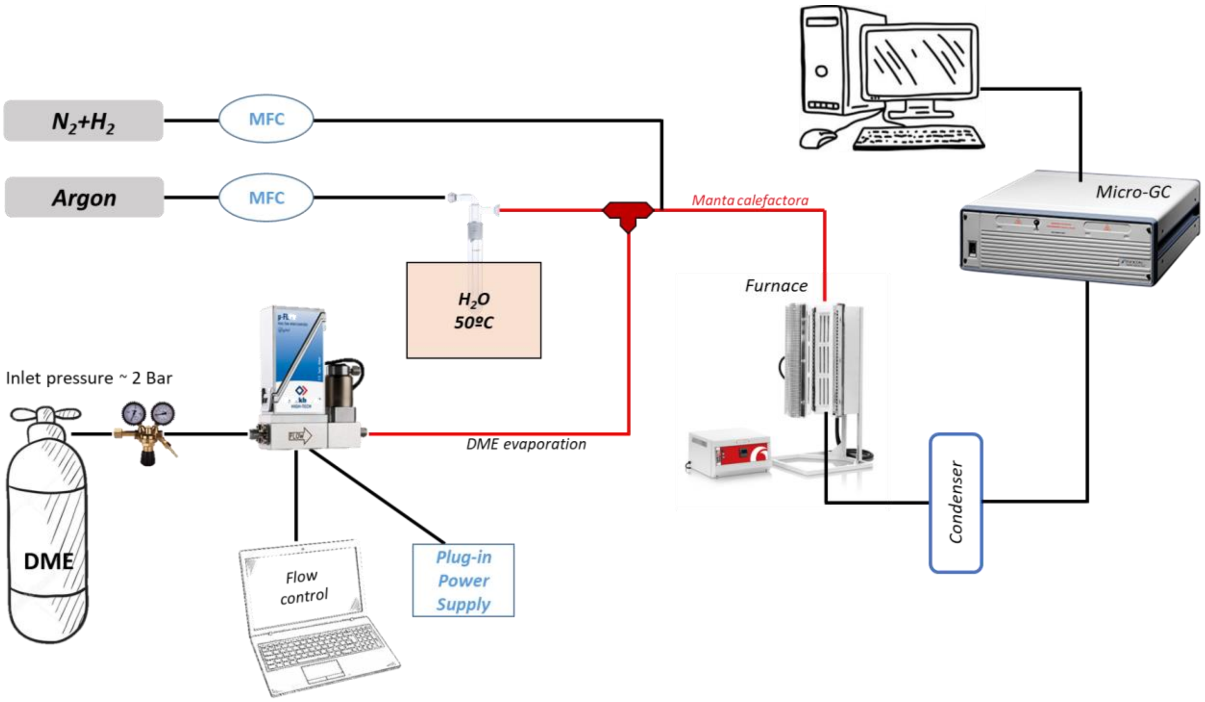

Figure 34- Set-up of steady state experiment

5.1.2 DME steam reforming

The reaction taking place inside the μ-reformer channels was the DME steam reforming. It is an endothermic reaction ($\Delta H_r^0 = 135\ \mathrm{kJ/mol}$) that requires relatively low temperature (350-500°C). Due to the use of water, is probable that water is adsorbed on the platinum hindering the DME and oxygen adsorption, resulting in lower conversion. It is preferred the DME to the methanol because of the easier handling. The infrastructure for store and manage the methanol safely are not well developed and also the toxicity of the methanol is high [29]. However, a good percentage of conversion can be reached. Even if the hydrogen production pass by the steam reforming of methanol, there is no storage for this gas. The methanol is produced and directly consumed by the reaction in order to produce hydrogen.

The DME conversion in hydrogen is not direct, it involves 2 reactions. The steps of the process are:

DME hydrolysis:

$$CH_3OCH_3 + H_2O = 2CH_3OH \tag{1}$$

Methanol steam reforming:

$$2CH_3OH + H_2O = CO_2 + 3H_2 \tag{2}$$

It is a two-step reaction facilitated by a bifunctional catalyst, descripted in section 3.1.3. However, depending on the catalyst deposited, some other side reactions can take place. For this experiment, the involved side reactions were:

DME thermal decomposition:

$$CH_3OCH_3 = CH_4 + CO + CO_2 \tag{3}$$

Water gas shift:

$$CO + H_2O = CO_2 + H_2 \tag{4}$$

Direct CO_2 formation:

$$CH_3OCH_3 + H_2O = CH_4 + CO_2 + 2H_2 \tag{5}$$

These three reactions are the most relevant and also are the side reactions considered in the FEM model [30].

5.2 SIMULATION MODEL

The simulation model was performed with the software COMSOL Multiphysics and the same conditions of the experimental test were adopted (section 5.1.1).

5.2.1 Geometry and mesh

The model was based on one of the several channel composing the central part of the suspended µ-reformer. It was analysed only one channel for make the simulation easier and faster. Nevertheless, this implies that all the channels worked in the same way, so the results obtained were multiplied by number of channels (7000 in this case). Thus, a 2D-axialsymetric FEM model was developed in order to evaluate and improve the efficiency of conversion of the DME in a hydrogen-rich fuel. According to the sample's dimension, the diameter of the channel was 50 µm and the length was 500 µm. Furthermore, it was added a 0.1 µm thick layer simulating the catalyst's thickness. The detail is shown in Figure 35.

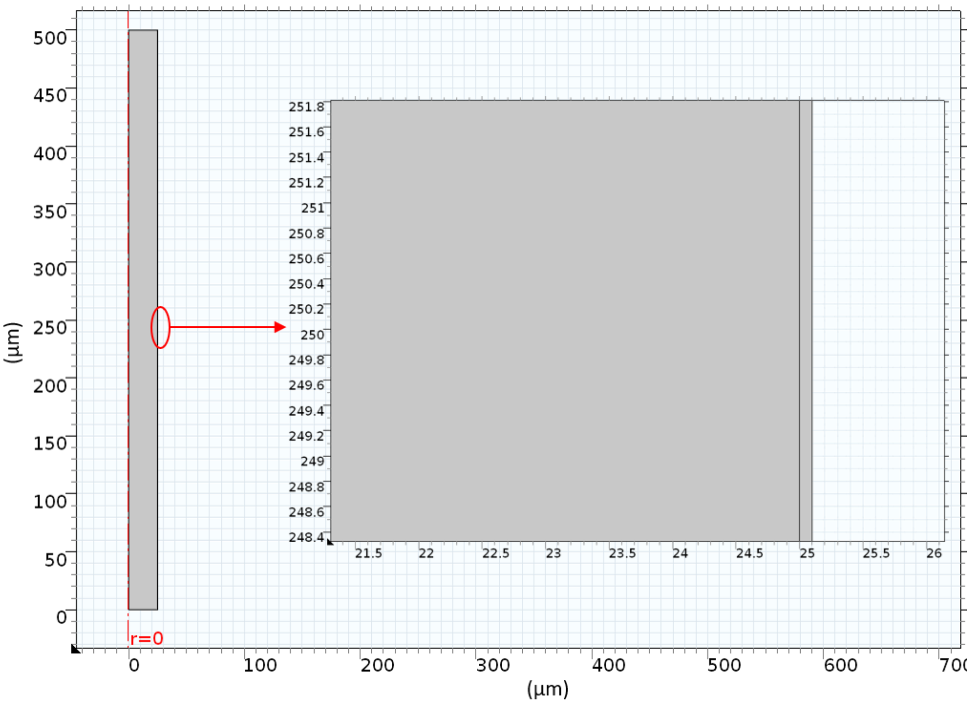

Figure 35-Geometry of the model

The chosen mesh of the domain is shown in Figure 36. It was chosen a mapped distribution since a laminar flow was involved (section 5.2.2.1). As it is visible from the detail in the picture, the nodes were concentrated mostly in the wall and in the entrance region because were the areas more involved in changings. The catalyst was deposited in the wall of the channel, so the wall was expected to be the most reactive region of the domain. While, in the entrance region the laminar flow was developing its profile.

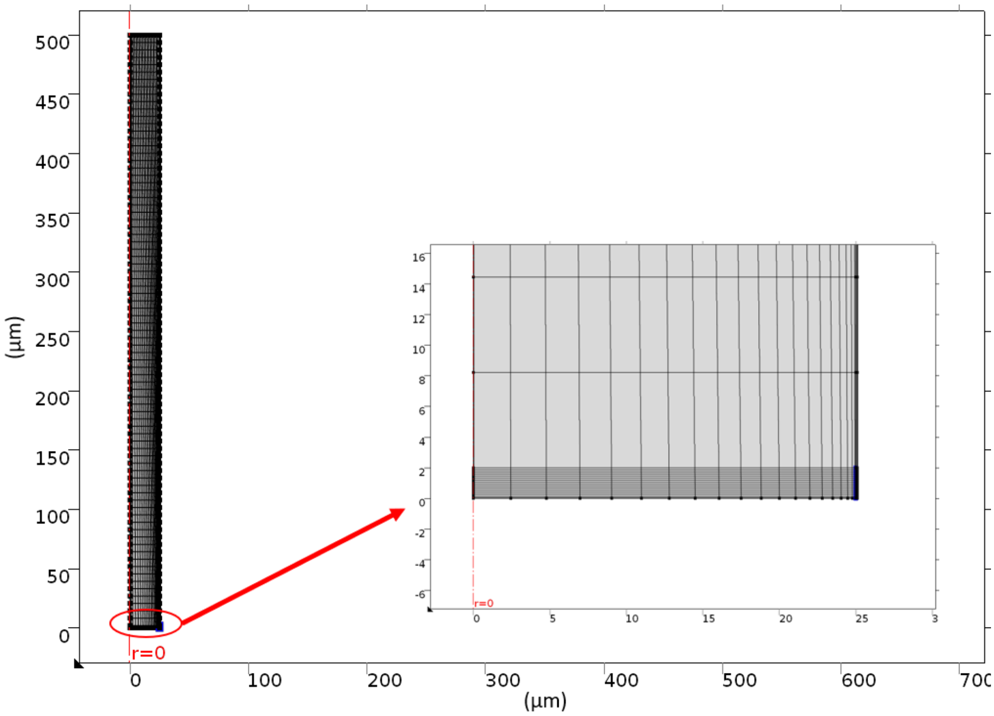

Figure 36- Mesh of the geometry

5.2.2 Physics

In order to creating a simulation, one of the most important step is defining the proper physics, including the appropriate constraints and parameters. In detail, the fluid dynamic was modelled with the *laminar flow* interface, the chemical reactions were modelled with the combination of *reaction engineering* and *transport of diluted species* interfaces and the energy balance was modelled with the *heat transfer in fluids interface*. In the following, a detailed description of each interface is presented.

5.2.2.1 Laminar flow

The laminar flow interface was used to compute the velocity and pressure fields in laminar condition. The flow was certainly laminar because the Reynold number is $1.28*10^{-2}$ and the critical value corresponding to the a turbulent flow in a pipe is 2300. The equations solved are the Navier-Stokes and the continuity equations. In particular, the equations governing the laminar flow were:

$$\rho(\boldsymbol{u} \cdot \Delta)\boldsymbol{u} = \Delta \cdot \left[-pl + \mu(\Delta\boldsymbol{u} + (\Delta\boldsymbol{u})^T) - \frac{2}{3}\mu(\Delta\boldsymbol{u})l\right] + F$$

$$\Delta \cdot (\rho\boldsymbol{u}) = 0$$

Where $\boldsymbol{u}$ is the velocity field, p is the pressure, μ is the dynamic viscosity, ρ is the density, F is volume force. It was assumed an axial velocity field, without any radial component.

In the inlet section was imposed the condition:

$$\boldsymbol{u} = -U_0 \cdot \boldsymbol{n} \cdot \frac{T}{T_0}$$

Where U_0 is the entering fluid velocity and was set to 0.03345 m/s, T is the entering flow temperature in Kelvin, T_0 is the reference temperature and is 300 K, $\boldsymbol{n}$ is unit vector of the inlet cross section.

Considering a stationary operation, the inlet velocity was depending on the temperature in order to respect the continuity equation:

$$\rho \cdot A \cdot \boldsymbol{u} = costant$$

Since the inlet cross section A was unchanged and the density (ρ) was changing according to the temperature, the velocity had to change to keep a constant value. The molar flowrate was constant because it wasn't depending on the temperature.

In the wall of the channel was assumed, due to the laminar flow, that the fluid was not moving. No slip condition was set:

$$\boldsymbol{u} = 0$$

While in the outlet section, a pressure condition was imposed:

$$\left[-pl + \mu(\Delta\boldsymbol{u} + (\Delta\boldsymbol{u})^T) - \frac{2}{3}\mu(\Delta\boldsymbol{u})l\right]\boldsymbol{n} = -p_0 \cdot \boldsymbol{n}$$

Where p_0 is the outlet pressure that was set equal to 1 bar.

The fluid properties were temperature-depending according to the temperature profile computed in the simulation.

Since the flow was laminar, the maximum velocity was in the centre of the channel and was the double of the average velocity:

$$u_{max} = 2 \cdot u_{ave}$$

5.2.2.2 *Reaction engineering*

The reaction engineering interface was used to model the reactor type and the reactions involved in the experiment. The reactor type chosen was a plug flow reactor governed by the following equations:

$$\frac{dF_i}{dV} = R_i \qquad c_i = \frac{p}{R_g\, T} \frac{F_i}{\sum_i F_i} \qquad v = \frac{R_g T}{p} \sum_i F_i$$

Where F_i is the molar flow of the ith specie, v is the total volume, R_i is the reaction rate of the ith specie, c_i is the molar concentration of the ith specie.

Perfect mixing was assumed to occur in the radial direction choosing this type of reactor, while temperature and concentration gradient were developed in the axial direction. The mixture entering the reactor was in gaseous state. The pressure of the reactor was set constant and equal to 1 bar. While the temperature was computed in another interface (section 5.2.2.4).

The reactions involved in the simulation, as described in section 5.1.2, were:

1. DME hydrolysis
2. Methanol steam reforming
3. DME thermal decomposition
4. Water gas shift
5. Direct CO_2 formation

The reactions were assumed to taking place only in the catalysed region, where the catalyst was deposited. The assumption was made because inside the catalysed region the reactions rates were much bigger with respect to the rest of the channel, along which the reactions rates were considered negligible. The considered region is shown in Figure 37.

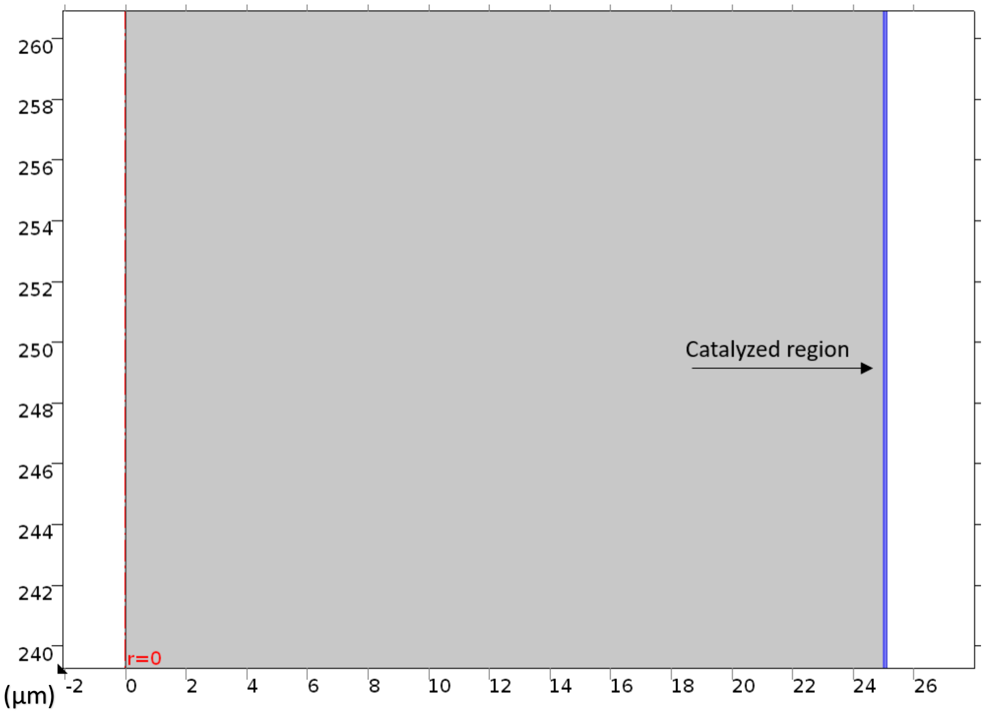

Figure 37-Site of the reactions

The equilibrium constant of each reaction was written in an Arrhenius form and characterized by a pre-exponential factor and an activation energy:

$$k_i = A_i \cdot \exp\left(-\frac{E_{a_i}}{R_g T}\right) \quad (1/s)$$

The values were based on literature with some adjustment related to the different catalyst and set-up of the experiment. The activation energy is the parameter most affected by the catalyst, in literature wasn't found a model reproducing the same composition of the catalyst used, so the values of E_a were manually modified in order to approach as much as possible the used composition. While, the pre-exponential factor is affected mostly by the set-up (i.e. porosity, active layer dimension, catalyst homogeneity), also in this case the values were changed for the same reason of the E_a. An analysis of the uncertainties obtained in the values adopted in the model is presented in Chapter 5.2.3.2.

Table 5 sums-up the final parameters compared with the reference literature:

Table 5- *Activation energies*

	Model values	*Literature values*
	E_a (kJ/mol)	E_a (kJ/mol)
1) DME Hydrolysis	165	145.1 [30]
2)MeOH steam reforming	82.5	84.1 [30]
3)DME thermal decomposition	190	176 [31]
4)Water gas shift	173	120 [32]
5)direct CO_2 formation	175.5	136 [33]

After defined all the equilibrium constant, the reaction rates were define as follow in Table 6:

Table 6- *Reactions rates*

	Reaction rate
1) DME Hydrolysis	$k_1 \cdot c_{H_2O} \cdot c_{CH_3OCH_3}$
2)MeOH steam reforming	$k_2 \cdot c_{H_2O} \cdot c_{CH_3OH}$
3)DME thermal decomposition	$k_3 \cdot c_{CH_3OCH_3}$
4)water gas shift	${k_4 \cdot c_{H_2O}}^{0.3}$ [32]
5)direct CO_2 formation	$k_5 \cdot c_{H_2O} \cdot c_{CH_3OCH_3}$

Finally, this interface was linked with the other physics involved using the "Generate Space-Dependent Model" tool, available in the software. In this way, the mass, energy and momentum balances were referred to the dynamics of the overall simulated model.

5.2.2.3 *Transport of diluted species*

The transport of diluted species interface was used to calculate the concentrations of the reformed flow, accounting for the production or the consumption of the species. The transports phenomena were governed by the Fick's law and the convection equation:

$$\Delta \cdot (-D_i \Delta c_i) + \boldsymbol{u} \cdot \Delta c_i = R_i$$

Where D_i is the diffusion coefficient of the ith specie, c_i is the molar concentration of the ith specie, R_i is the reaction rate of the ith specie. The first term is the contribution of the Fick's law, the second is the contribution of the convection.

The diffusion coefficients of all the species were estimated as follow [34]:

$$D_{A/B} = \frac{0{,}00155 \cdot T^{1.5} \cdot \left(\frac{M_A + M_B}{M_A \cdot M_B}\right)^{0.5}}{P \cdot \left(V_A^{\frac{1}{3}} + V_B^{\frac{1}{3}}\right)^2}$$

Where $D_{A/B}$ is the diffusivity of the component A in the mixture A+B, M_A and M_B are the molecular weight of the components, V_A and V_B are the molecular volume, P is the pressure of the mixture.

The species entering the system were DME (CH_3OCH_3) and the carrier gas (Ar). Steam was entering the system mixed in Argon (12.2% of the entering Argon flow). The molar volumetric concentration (mol/m^3) was requested as input in the model, but the volumetric flowrate (ml/min) was measured in the experiment. Thus, assuming the hypothesis of ideal gas and knowing that the volume occupied by a mole of ideal gas is 22.414 l/mol in standard condition, the conversion was computed as follow:

$$\left(\frac{\boldsymbol{ml}}{\boldsymbol{min}}\right) \cdot 10^{-6} \left(\frac{m^3}{ml}\right) \cdot \frac{1}{0.022414 \cdot \frac{T}{273}} \left(\frac{mol}{m^3}\right) \cdot \frac{1}{\dot{V}} \left(\frac{min}{m^3}\right) = \left(\frac{\boldsymbol{mol}}{\boldsymbol{m^3}}\right)$$

Where $\dot{V}$ is the total entering volumetric flowrate. It was also considered the dependence on the temperature of the volume occupied by a mole of ideal gas.

Table *7* resumes the obtained conversion results, DME/steam ratio is equal to 6.

Table 7- Entering flow rate and concentration

	Volumetric flowrate (ml/min)	*Molar volumetric concentration (mol/m^3) @300 K*
Argon	24.6	31.8
of which steam	3	4.42
DME	0.5	0.736

However, the molar volumetric concentration was also inversely depending on the temperature of the mixture:

$$c_1 = c_0 \cdot \frac{T_0}{T_1}$$

Finally, in the outlet boundary was assumed convection as dominating transport mechanism, so the diffusive transport phenomenon was ignored:

$$-\boldsymbol{n} \cdot D_i \, \nabla c_i = 0$$

5.2.2.4 Heat transfer in fluids

The heat transfer in fluids interface was used to model the heat transferred by convection. The equation governing the heat transfer was:

$$\rho C_p \boldsymbol{u} \cdot \Delta T = \Delta \cdot (k \Delta T) + Q$$

Where ρ is the mixture density, C_p is the heat capacity, *T* is the absolute temperature, *k* is the thermal conductivity, *Q* is the volumetric heat generated.

The active area of the sample was assumed to be at constant temperature because it was made on Silicon and also was thermally insulated from the chip by the air trench. This assumption implied, as a consequence, that the wall of the channel was at constant temperature:

$$T = T_{wall}$$

It was also assumed that the temperature of mixture entering the channel was homogeneous and constant, so the inlet section of the channel was also set at constant temperature:

$$T = T_{mix,in}$$

In order to perform the energy balance, the enthalpy of reaction was considered. Multiplying the enthalpy of reaction by the reaction rate it was evaluated the volumetric heat generated or requested:

$$Q_i = -r_i * H_i \qquad \left(\frac{\mathrm{W}}{\mathrm{m}^3}\right)$$

Where r_i is the reaction rate and H_i is the enthalpy of reaction. The overall process was endothermic.

In the outlet boundary was assumed that the heat was transferred only by convection, the gradient of temperature in the normal direction is equal to zero:

$$-\boldsymbol{n} \cdot (-k\Delta T) = 0$$

5.2.3 Results

For all the reported results was considered the micro-reformer active area temperature of 923 K (650°C). Thus, T_{wall} was set equal to 923 K.

The obtained velocity field (Figure 38) shows the expected development of the laminar flow. There is a first entrance region where the flow is not developed and is changing the profile. Due to the low velocity, the entrance region is very short and also the flow is following a ordered path without any lateral mixing. After this first region, the flow is fully developed and the profile no more changes along the remaining length of the channel. The velocity is zero when the fluid is passing on the wall of the channel and is maximum in the centre. At 923 K, the inlet velocity was 0.11 m/s and thus the maximum central velocity was 0.22 m/s. Considering this velocity, the Reynolds number is $8.42*10^{-2}$, thus the laminar flow condition is still verified.

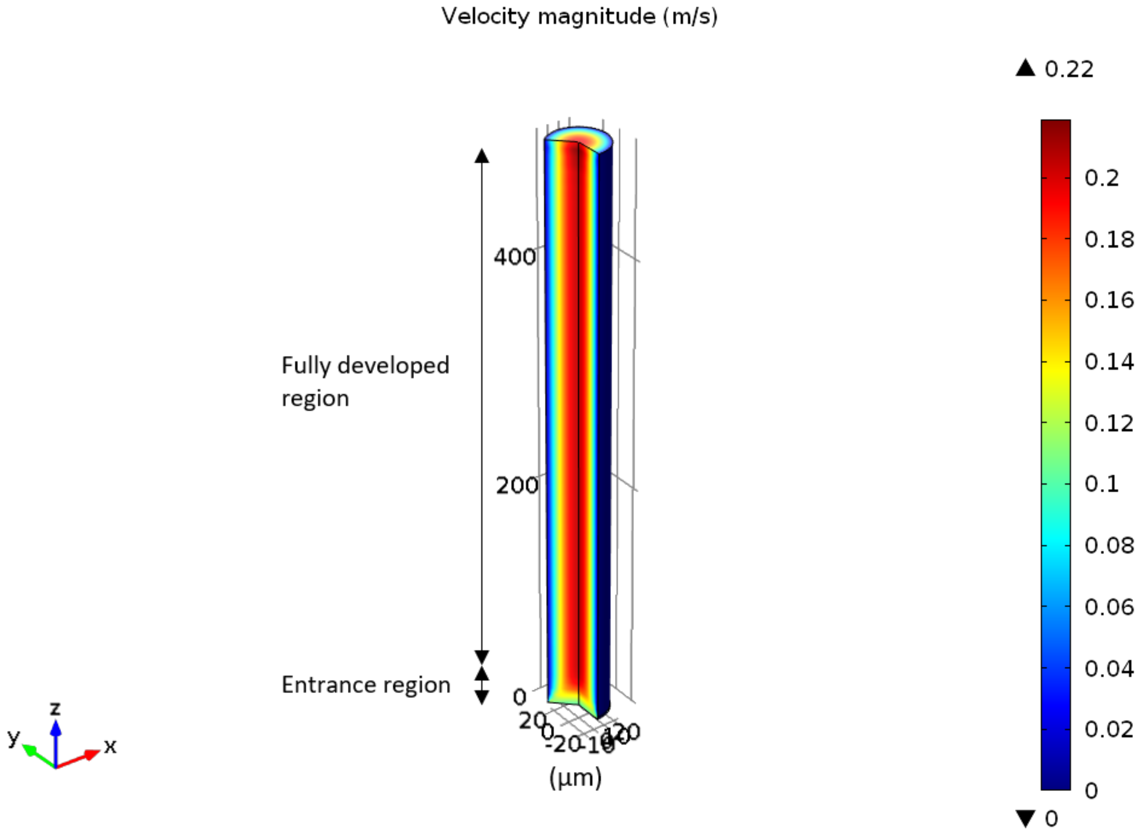

Figure 38- Velocity field

Assuming an inlet flow temperature ($T_{mix,in}$) of 400 K (127 °C), the temperature distribution is shown in Figure 39. Also in this case there was a short entrance region in which the temperature was changing and then a fully developed region. In this case the shape of the temperature distribution profile was depending on the wall temperature and the heat fluxes involved. In the centre of the channel there should have been the minimum value of temperature since the wall was kept at a constant higher temperature than the entering flow. Nevertheless, in this case due to the low velocity of the incoming flow and to the small dimension of the channel, the mixture was characterized by a constant and homogenous distribution of the temperature.

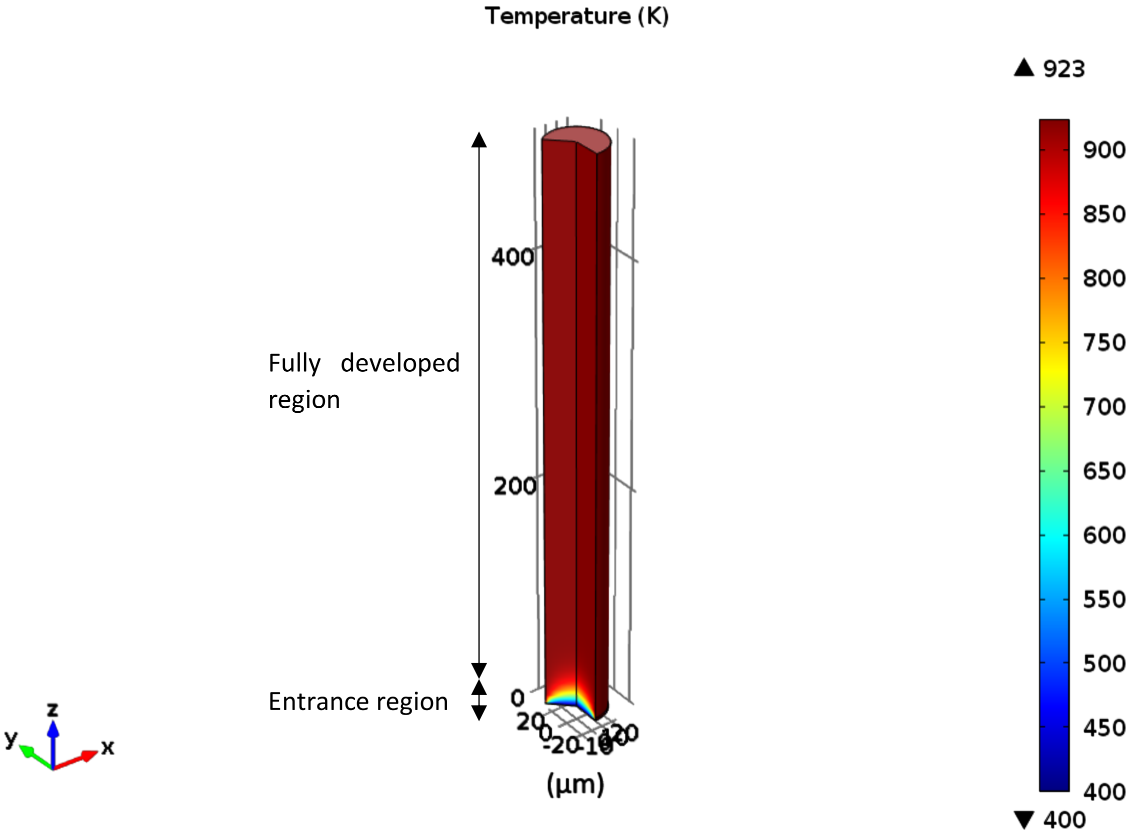

Figure 39- Temperature distribution

The concentration of hydrogen and DME are shown in Figure 40. Regarding the hydrogen, in the first part of the channel the concentration was zero and was increasing along the length of the channel. This is the expected trend since the hydrogen was not entering the system, it was only produced by the chemical reactions. Otherwise, the DME was entering the system and reacting along the channel thus the concentration is decreasing. One important difference between the two distribution is visible in the diffusion mechanism of the two species. Due to the fact that hydrogen was characterized by a diffusion coefficient one order of magnitude larger than all the other species, in its distribution is almost no more visible the velocity profile. The concentration is increasing almost homogeneously along the length of the channel. While in DME distribution is rather visible the velocity profile, in fact it was consuming more rapidly near the wall of the channel because the velocity tended to zero going toward the wall. For the DME the diffusion coefficient was not enough for allowing a homogenization of the concentration.

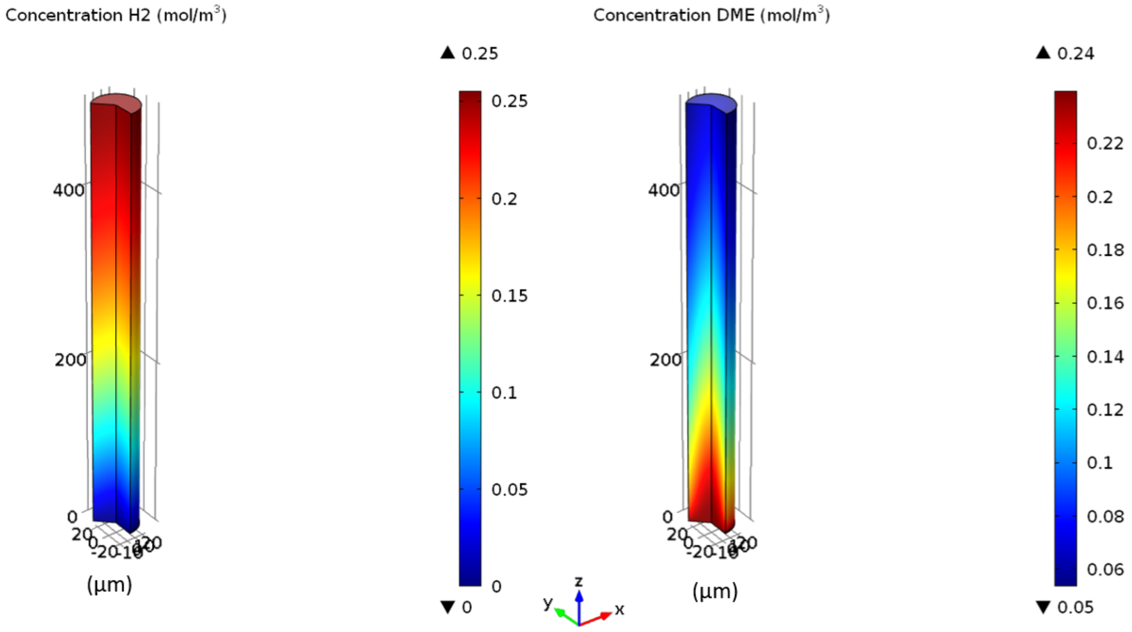

Figure 40- concentration of hydrogen and DME

The hydrogen reaction rate is shown in Figure 41. As reasonable, the reaction rate was concentrated only in the wall of the channel because all the involved chemical reactions were taking place only there. The value of the hydrogen reaction rate was decreasing along the channel because it was depending on the concentration of reactants (as defined in 5.2.2.2), since the only reactant was DME and its concentration was decreasing as shown in Figure 40, the reaction rate was decreasing.

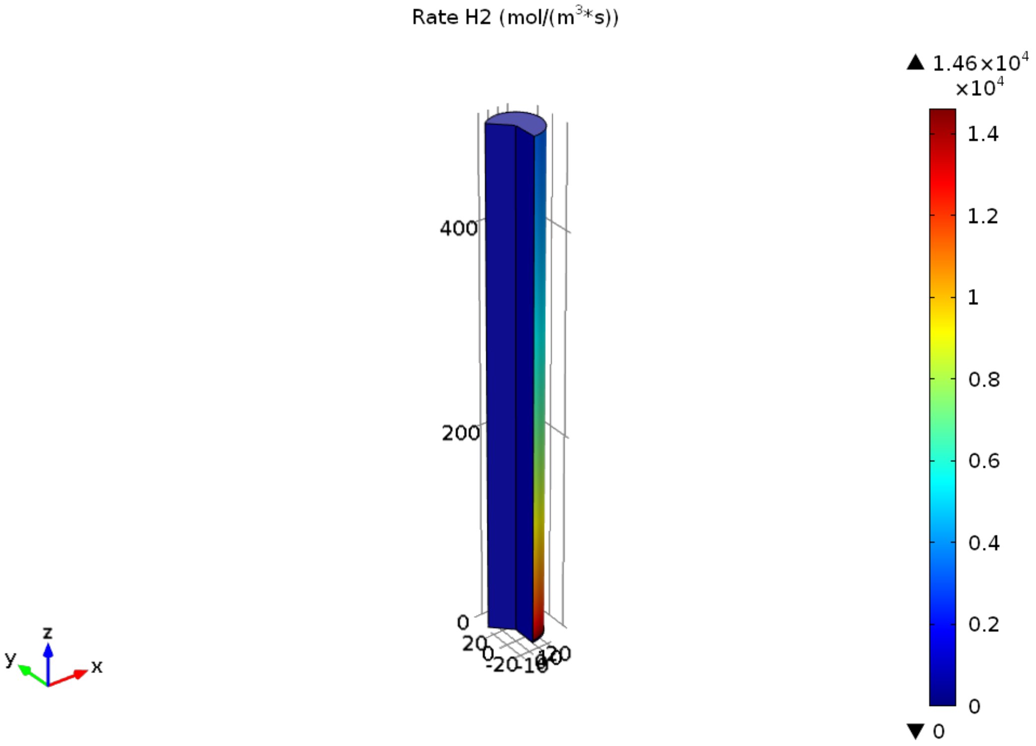

Figure 41- Rate of reaction of hydrogen

5.2.3.1 *Experimental comparison*

In order to validate the model, the results obtained from the model simulation were compared with the experimental results. A “parametric sweep” analysis was performed on COMSOL to obtain the results. This tool allows solving a sequence of problems by varying one or more parameters of interest. In this case, the interested parameter was the temperature. The considered range of temperature was the same of the experimental, from 450°C to 650°C (723 K to 923 K).

The comparison was made firstly in term of percentage of DME conversion and then were also compared the percetanges of the reformed exitnig gases. The exiting gases were H_2, CO, CH_4, CO_2.

However, the first and most important comparison taken in account was the DME conversion trend. The conversion percetenage was calcualted by consdering the molar flow as follow:

$$\%_{DME,reacted} = \frac{mol_{DME,in} - mol_{DME,out}}{mol_{DME,in}} \cdot 100$$

The molar flow entering and exiting the channel was calculated by computing a 2D integral of the “normal total flux” (mol/(m^2*s)) in the two section of the channel. This calculation was reapetd for each temperature considered in the parametric sweep mentioned before.

The results are shown in Figure 42. It was found a good descpription of the esperimental curve that preseted an Arrenhius form. The range between 830 K and 880 K shows the biggest deviation of the model curve from the experimental, nevertheless the percentages devitation is around 10%. Also for low temperature there is a little deviation in the converion, but is limitated to an error of around 5%.

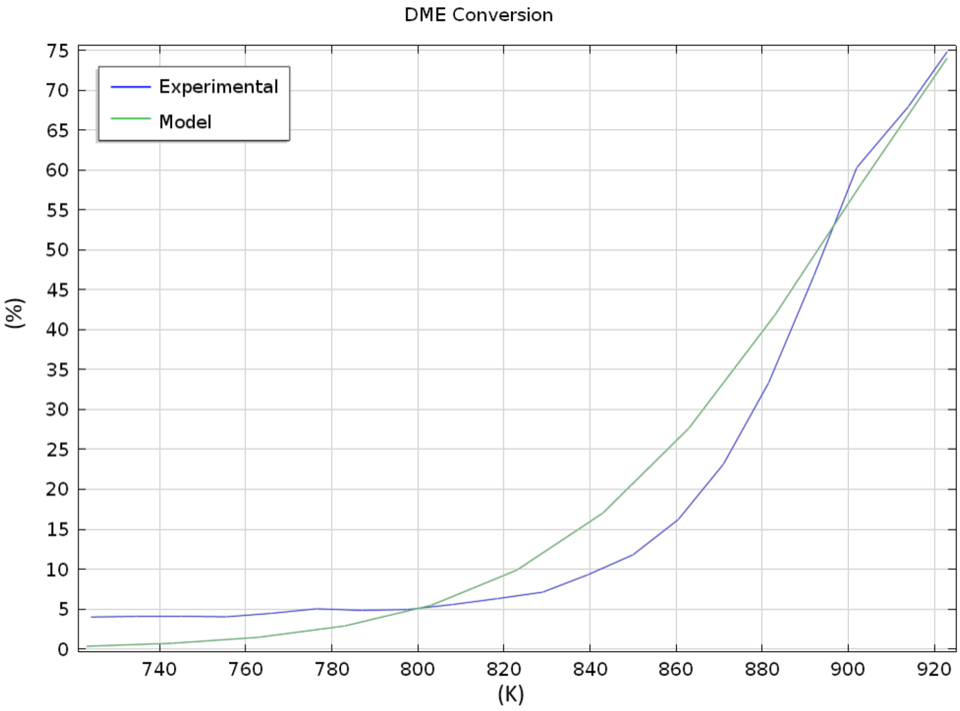

Figure 42- DME conversion comparison

Regarding the exiting reformed gases, it was calculated a relative percentage with respect to the percentage of reacted DME:

$$\%_{DME,reacted} \cdot \frac{mol_{i,out}}{mol_{tot,out}} \cdot 100$$

Where $mol_{i,out}$ is the molar flow of the ith exiting gas and $mol_{tot,out}$ is the sum of all the exiting gases excluded Argon and steam. Also in this case the molar exiting flows of the various gases were calculated with the 2D integral of the “normal total flux” in the outlet section of the channel. Also in this case, the calculation was reapetd for each temperature considered in the parametric sweep mentioned before.

The comparison of the hydrogen produced is reported in Figure 43. Also in this case the larger deviation between the two curves is in the range between 830 K and 880 K, but the larger values is about 5% in the maximum point.

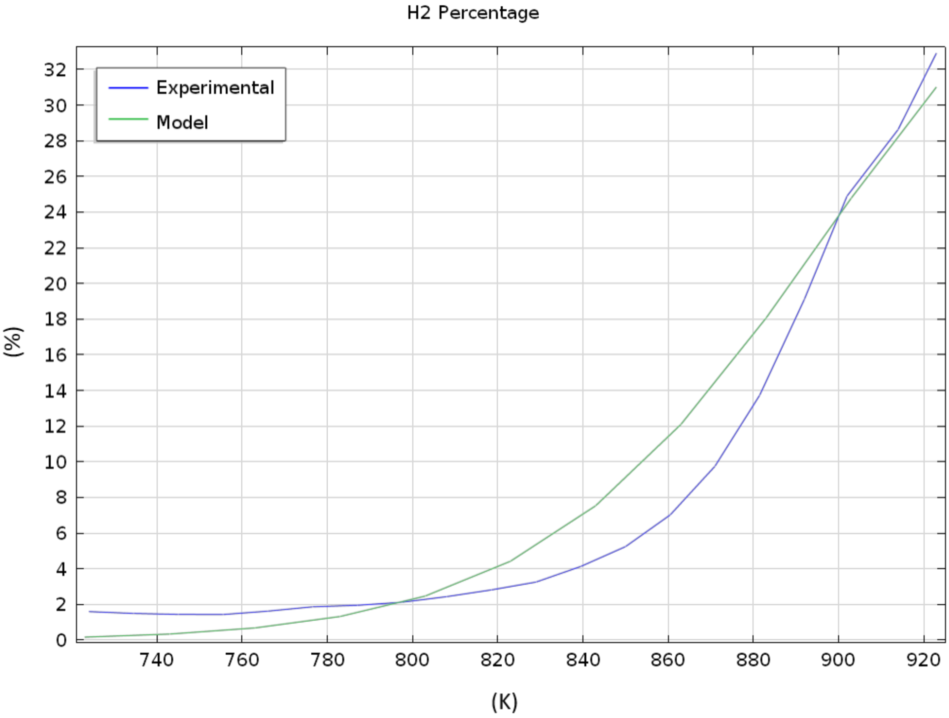

Figure 43- Hydrogen percentage comparison

The comparison of the reformed CO,CO$_2$ and CH$_4$ are showed in Figure 44. It was obtained a good fitting also in these cases. In the case of the CO2 there was a larger deviation in the lower temperature range until 820 K with a value of around 2%. Also for the CO the maximum error was around the 2% in the range 840-880K. While the CH$_4$ showed a maximum deviation of around 4% in the same range of the CO.

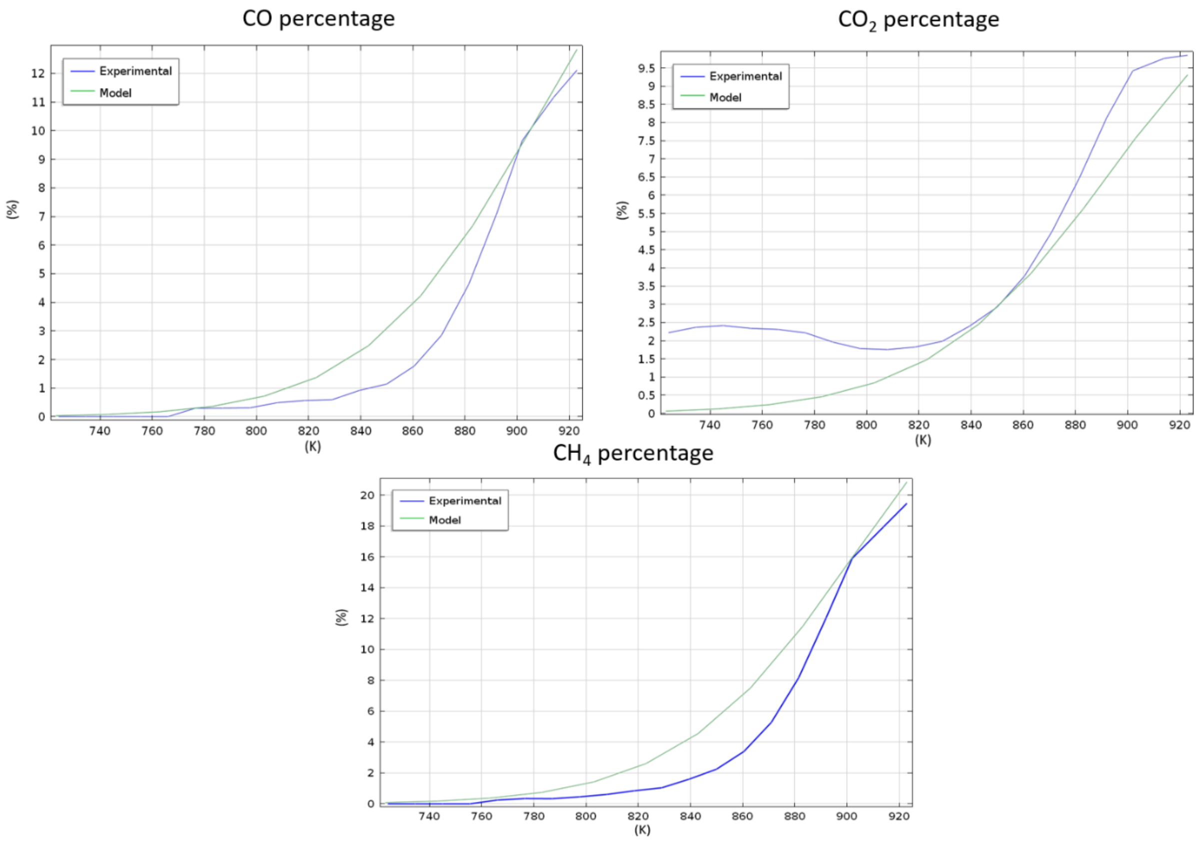

Figure 44-CO,CO$_2$,CH$_4$ conversion comparison

The final composition of the exiting mixture is shown in Figure 45. As expected, the main component of the mixture was hydrogen because of the use of the catalyst. Always because of the catalyst there was a significant amount of CO and CH_4 as side product. They can also be used as fuel for the µ-SOFC. The methanol (CH_3OH) is also reported in the graph, but the percentage is negligible with respect to the all species. The methanol is produced from the hydrolysis of the DME but it is almost totally consumed by the methanol steam reforming reaction. The evolution of all the species was following a Arrhenius trend and the total usable percentage of reformed products is almost the 70% at 923 K.

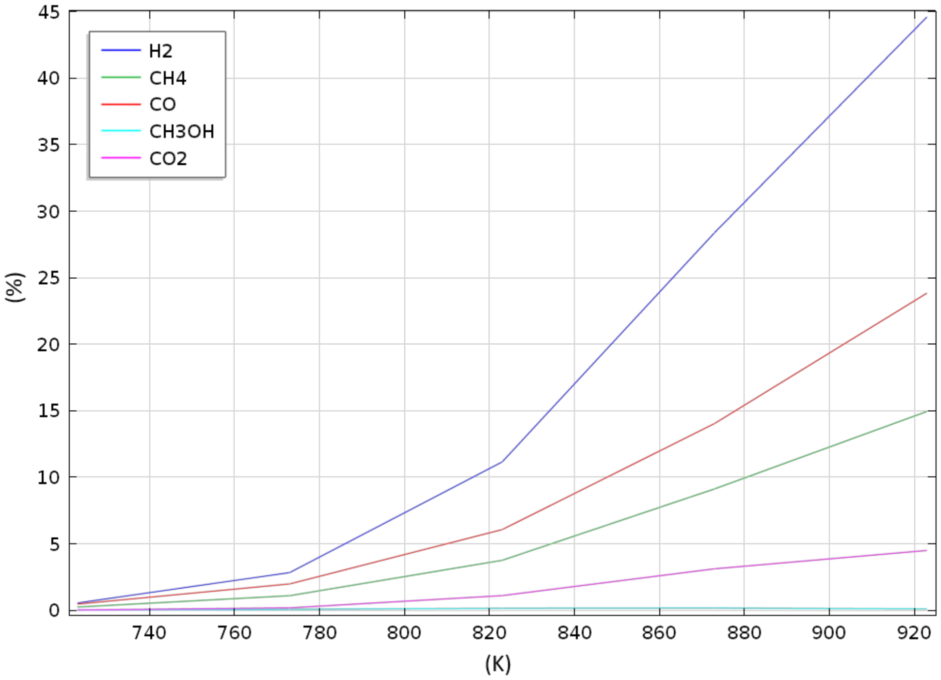

Figure 45- Composition of exiting flow

5.2.3.2 Error evaluation

After the comparison with the experimental results, it was performed an error evaluation for justifying the choice of the activation energies of the involved reactions. The values were changed starting from the literature values in order to fit the experimental curves as much as possible.

Firstly, was performed a sensitivity analysis involving 5 parameters: temperature and 4 activation energies. The activation energy of the water gas shift reaction was not included. Then it was calculated the relative error with respect to the experimental solution for each possible combination between these 5 parameters as follow:

$$err_{relative,i} = \left| \frac{\%_{DME,reacted,model,i} - \%_{DME,reacted,experimental,i}}{\%_{DME,reacted,experimental,i}} \right|$$

The relative error was based on the conversion percentage of the DME, considered as the most relevant parameter.

After the computation of all the relative error, it was calculated an average relative error for each temperature considering the same combination of the activation energies, the procedure is resumed in Table *8*.

The legend of the subscript number of each activation energy is:

1. DME hydrolysis
2. Methanol steam reforming
3. DME thermal decomposition
4. Water gas shift
5. Direct CO_2 formation

Table 8 - *Average error evaluation*

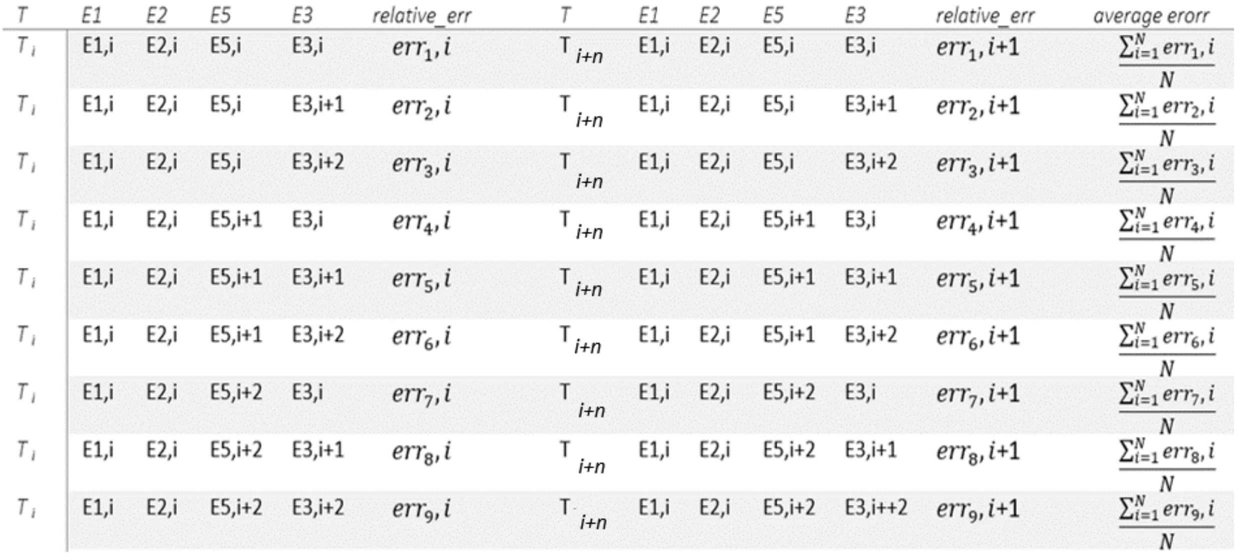

T	E1	E2	E5	E3	relative_err	T	E1	E2	E5	E3	relative_err	average erorr
T_i	E1,i	E2,i	E5,i	E3,i	err_1, i	T_{i+n}	E1,i	E2,i	E5,i	E3,i	$err_1, i+1$	$\frac{\sum_{i=1}^{N} err_1, i}{N}$
T_i	E1,i	E2,i	E5,i	E3,i+1	err_2, i	T_{i+n}	E1,i	E2,i	E5,i	E3,i+1	$err_2, i+1$	$\frac{\sum_{i=1}^{N} err_2, i}{N}$
T_i	E1,i	E2,i	E5,i	E3,i+2	err_3, i	T_{i+n}	E1,i	E2,i	E5,i	E3,i+2	$err_3, i+1$	$\frac{\sum_{i=1}^{N} err_3, i}{N}$
T_i	E1,i	E2,i	E5,i+1	E3,i	err_4, i	T_{i+n}	E1,i	E2,i	E5,i+1	E3,i	$err_4, i+1$	$\frac{\sum_{i=1}^{N} err_4, i}{N}$
T_i	E1,i	E2,i	E5,i+1	E3,i+1	err_5, i	T_{i+n}	E1,i	E2,i	E5,i+1	E3,i+1	$err_5, i+1$	$\frac{\sum_{i=1}^{N} err_5, i}{N}$
T_i	E1,i	E2,i	E5,i+1	E3,i+2	err_6, i	T_{i+n}	E1,i	E2,i	E5,i+1	E3,i+2	$err_6, i+1$	$\frac{\sum_{i=1}^{N} err_6, i}{N}$
T_i	E1,i	E2,i	E5,i+2	E3,i	err_7, i	T_{i+n}	E1,i	E2,i	E5,i+2	E3,i	$err_7, i+1$	$\frac{\sum_{i=1}^{N} err_7, i}{N}$
T_i	E1,i	E2,i	E5,i+2	E3,i+1	err_8, i	T_{i+n}	E1,i	E2,i	E5,i+2	E3,i+1	$err_8, i+1$	$\frac{\sum_{i=1}^{N} err_8, i}{N}$
T_i	E1,i	E2,i	E5,i+2	E3,i+2	err_9, i	T_{i+n}	E1,i	E2,i	E5,i+2	E3,i++2	$err_9, i+1$	$\frac{\sum_{i=1}^{N} err_9, i}{N}$

Finally, it was mapped the average relative error in function of the four activation energies. In Figure 46 is represented the error colour map. In each graph E_1 is the x-axis and E_3 is in the y-axis, while in the outer axis is changing E_2 in the upper part and E_5 in the left part. According to the colour legend, the values with red colour were characterized by a larger error, then the error was decreasing going to the blue colour. While, the black value is the one characterized by the lowest value of relative error, in fact was the chosen combination among all the other possible. These results shows that the obtained activation energies present the best fitting of the experimental values with an uncertainty of about 10%.

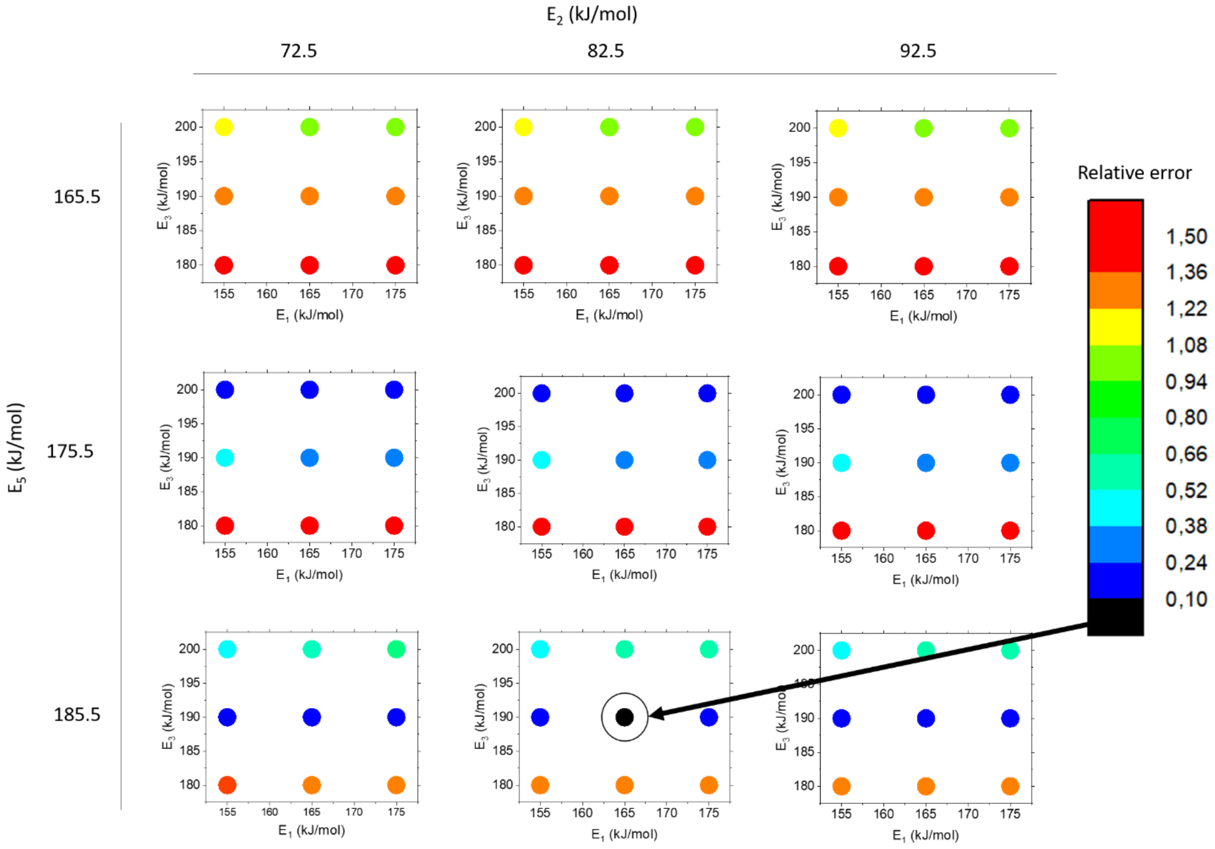

Figure 46-Error evaluation colour ma

5.2.3.3 Grid independence

As final validation for the model, was performed a grid independence analysis for removing the subjectivity of the solution. By changing the number of nodes in the mesh of the domain (the channel), was analysed how was changing the percentage of DME conversion at 923 K. As visible in Figure 47, the considered value was not changing anymore starting from almost 4000 nodes, nevertheless the difference with 2000 nodes was almost negligible. The chosen mesh was comprising almost 2000 nodes. It was chosen this value for made the simulation faster to converge. Thus, the solution can be consider as mesh independent because it wasn't relied on the type of mesh used.

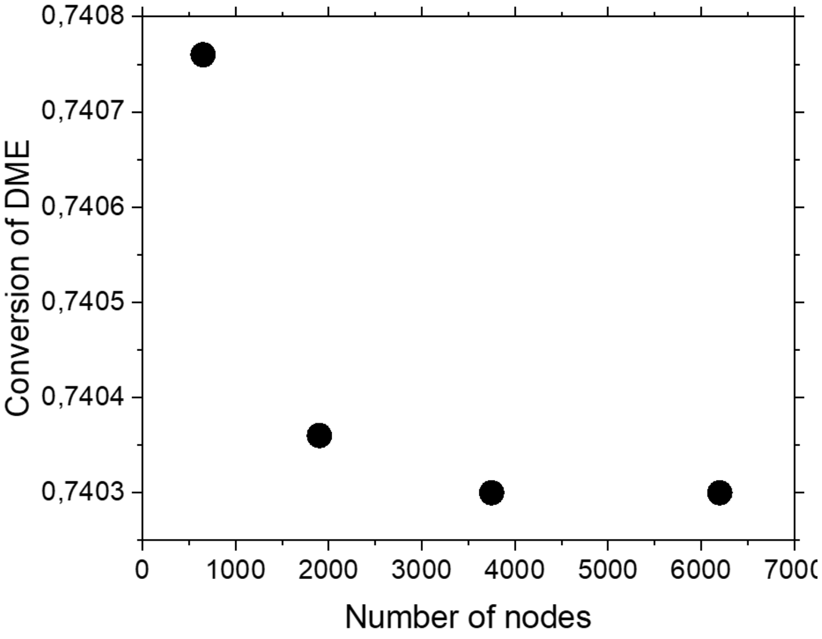

Figure 47- Grid independence

5.3 OPTIMIZATION

5.3.1 Chosen parameter

After the model was concluded, an optimization study was carried out. Unlike the previous case, for the optimization study the model was not compared with any experimental data. The optimization was performed with the aim of improving the DME conversion and the hydrogen production by changing the geometry of the channel and also the flow of the fuel.

The analysis was focused on varying the length and the radius of the channel and also the entering flow rate, the values are reported in Table *9*:

Table 9- *Optimization parameters*

Flow rate	*Length of the channel (µm)*	*Radius of the channel (µm)*
In the range $0.6*V_0$ - $3*V_0$ V_0=25.1 ml/min	250	25
	500	50
	1000	100

The underlined values in Table *9* were referred to the experimental case. The radius is the only parameter that was only increased because, due to the limit of the technologies for micro-fabrication, 25 µm was the minimum achievable radius.

5.3.2 Result

For the optimization was assumed a constant temperature of the µ-reformer active area of 923 K. Thus, all the reported graphs and comparison are referred to this temperature.

First, the dependence of DME conversion on the length of the channel was analysed. The trend is shown in Figure 48. The DME conversion increases according to the increase of the length of the channel. By doubling the length of the channel, the conversion reached almost the 95%. This trend can be justified by the increase of the catalyst active area. By doubling the length, theoretically, also the catalyst should be doubled, so was possible to convert almost completely the DME flowing in the channel. With a length of 1500 µm (3 times the original length) the conversion was close to 100%.

In this section, the red star in the graphs highlights the experimental parameters.

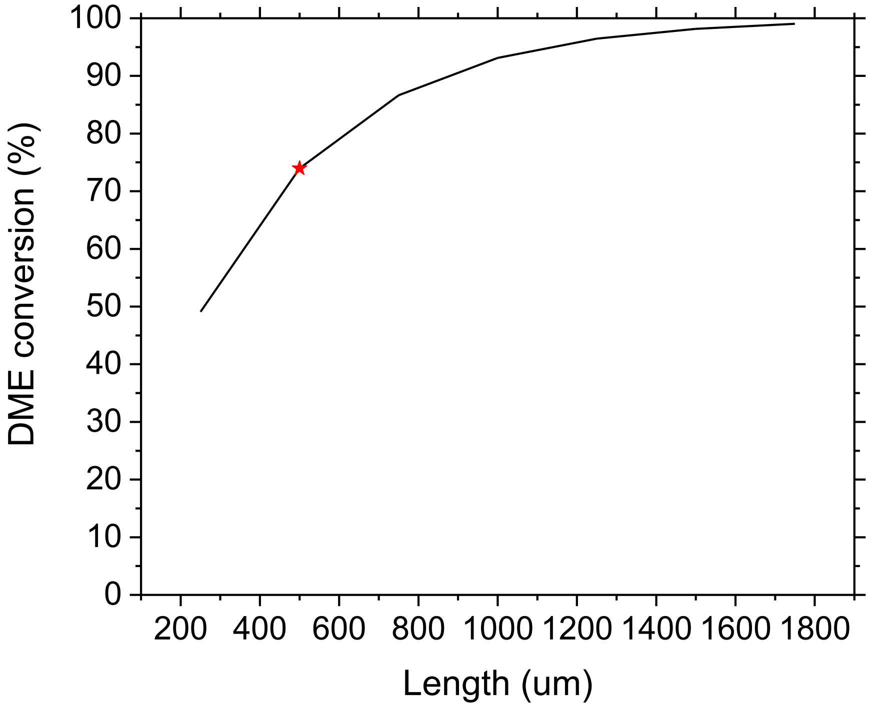

Figure 48- Length dependence for DME conversion

The hydrogen production, reported as µmole/second in the y axis in Figure 49, showed the same trend for the same motivation of the DME conversion.

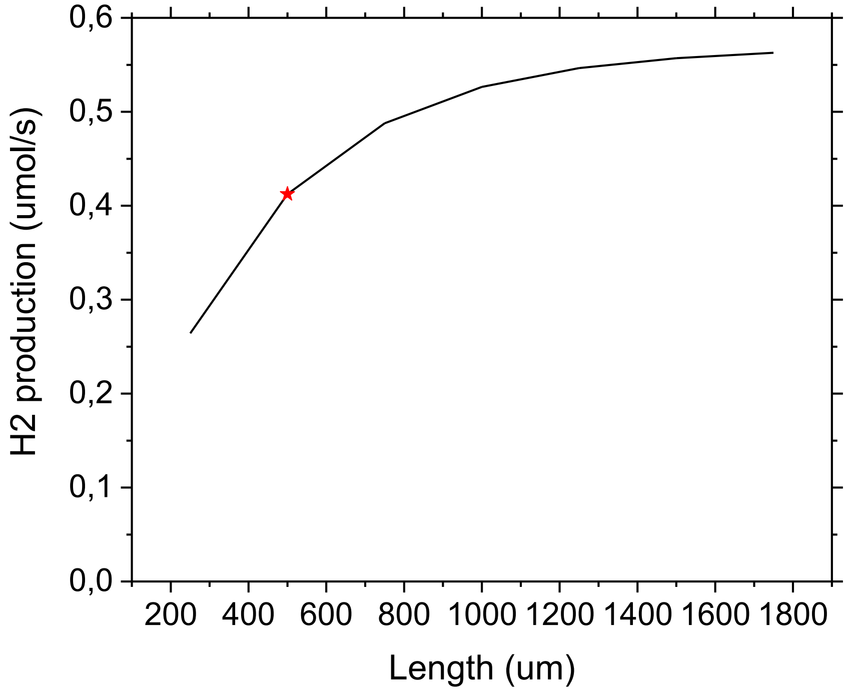

Figure 49- Length dependence for hydrogen production

Then it was analysed the dependence on the radius of the channel. It is important to notice that, by changing the dimension of the radius, it was also changed the number of channels in the active area. It was supposed a linear dependence between the two parameters. For example, doubling the radius halved the number of channels. This consideration was not necessary in the case of the length because the distribution of the channel was the same for every considered length.

Figure 50 shows the DME conversion depending on the radius. As visible, it was present a maximum point of conversion corresponding to a radius of 5 µm, but all the radius smaller than 25 µm were not taken in account in the optimization because of the technological limit. However it was reported the complete trend for a theoretical verification. The maximum point of conversion was depending on two factors: the thickness of the catalyst layer and the diffusion mechanism. The diffusion mechanism was responsible of spread the products of the catalysed reactions toward the centre of the channel. Since the properties of the catalytic layer were fixed, by increasing the radius more than 5 µm the diffusion mechanism was no more able to diffuse the products of the reaction as fast as they were produced, so the DME conversion lowered. Nevertheless, the DME conversion was sufficiently high also with the experimental radius.

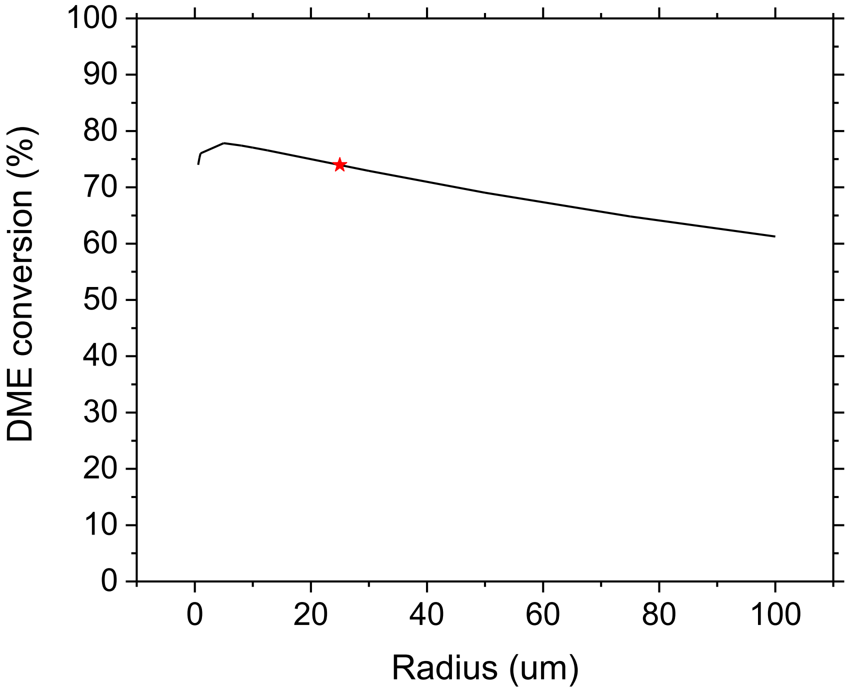

Figure 50- Radius dependence for DME conversion

The hydrogen production trend is shown in Figure 51. The production was increasing going towards smaller radius. This trend can be justified by the increasing of the catalysed area. By reducing the radius, the number of the channel was increasing, thus, if the radius was tending to zero, the catalysed area was tending to the total active area leading to an increase of the hydrogen produced. This increasing was also related to the velocity of the entering flow. A higher velocity was penalizing the DME conversion percentage, but was improving the hydrogen production. For better understand this motivation, a flow rate optimization analysis was performed.

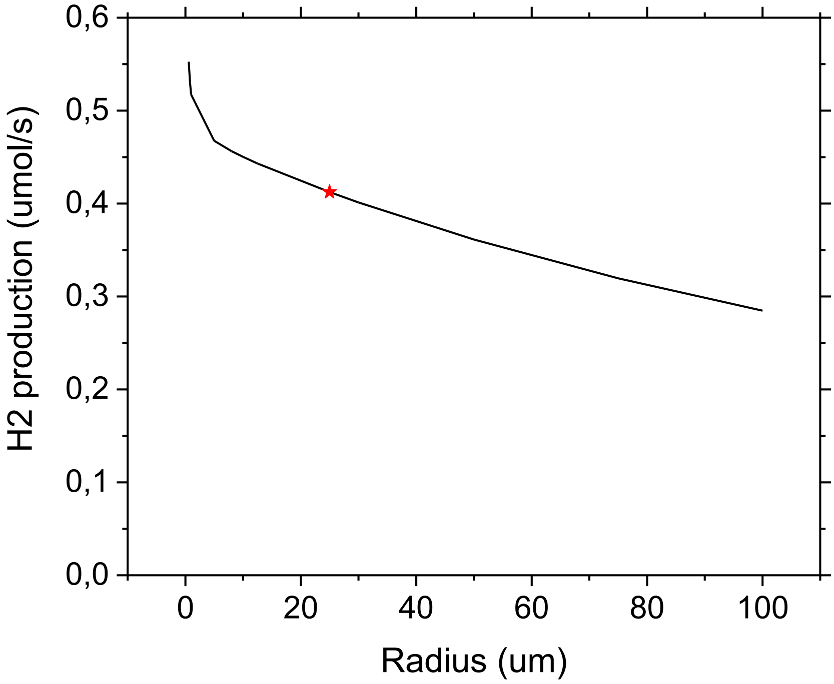

Figure 51- Radius dependence for hydrogen production

After the study of the geometrical parameters, it was carried out a study on the flow rate dependence. The comparisons were based on the radius dependence on the DME conversion and hydrogen production, but with different flow rate. The chosen flow rate range was between $0.6*V_0$ and $1.4*V_0$ (V_0=25.1 ml/min), it was considered a deviation of ±40% of the experimental value.

Firstly, was considered the DME conversion dependence, the results are shown in Figure 52. The blue curve represents the experimental case showed in Figure 50, but were not reported the radius smaller than 25 µm. There is a significant difference in the percentage of DME conversion in the 3 cases. By increasing the value of the flowrate, the DME conversion was reduced. The reduction was caused by the increase of the inlet velocity of the mixture. The volumetric flow rate is defined as follow:

$$\dot{V} = A * v$$

Setting constant the value of the inlet section (A), an increase of flow rate was corresponding to an increase of velocity. However, the conversion of DME was negatively affected from this parameter because, due to the higher flow velocity, it was less likely that the reaction took place. Also the diffusion mechanism was negatively affected.

While, reducing the flow rate value was corresponded to a reduction of the flow velocity, thus, the DME conversion was favoured.

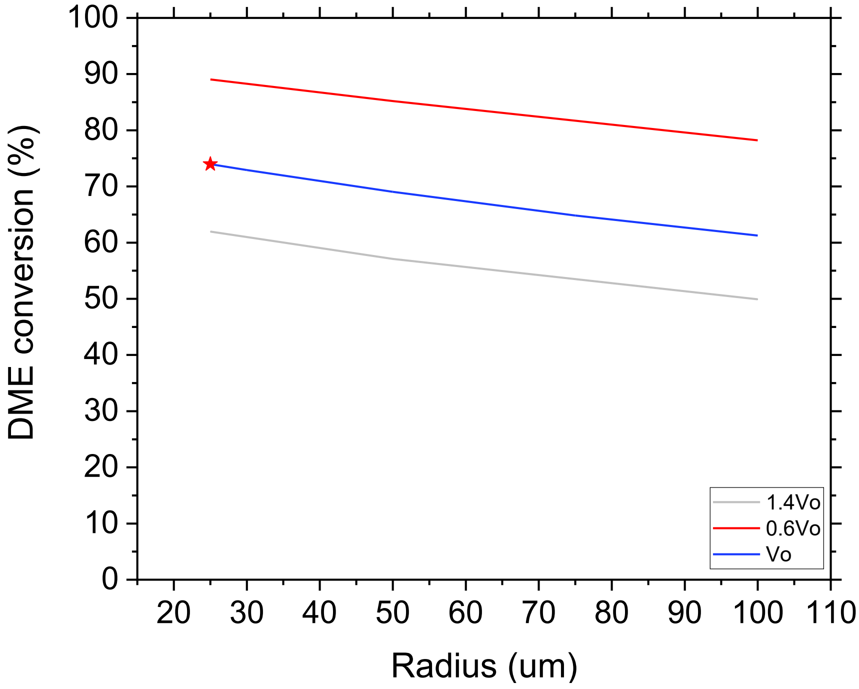

Figure 52- Flow rate dependence for DME conversion

Differently from the DME conversion, the hydrogen production showed an opposite trend, shown in Figure 53. Also in this graph, the blue curve is the same of the Figure 51 considering only the value larger than 25 µm. In this case, the production of hydrogen was favoured by the increase of the flow rate because, even if the conversion of DME was decreased, the number of moles of reactants introduced in the channel were increased. Thus, a smaller percentage of DME conversion was corresponding to a higher number of hydrogen moles produced. As final result, the increase of the flow rate was a positive effect for the production of hydrogen. As consequence, a smaller flow rate was penalizing the production of hydrogen.

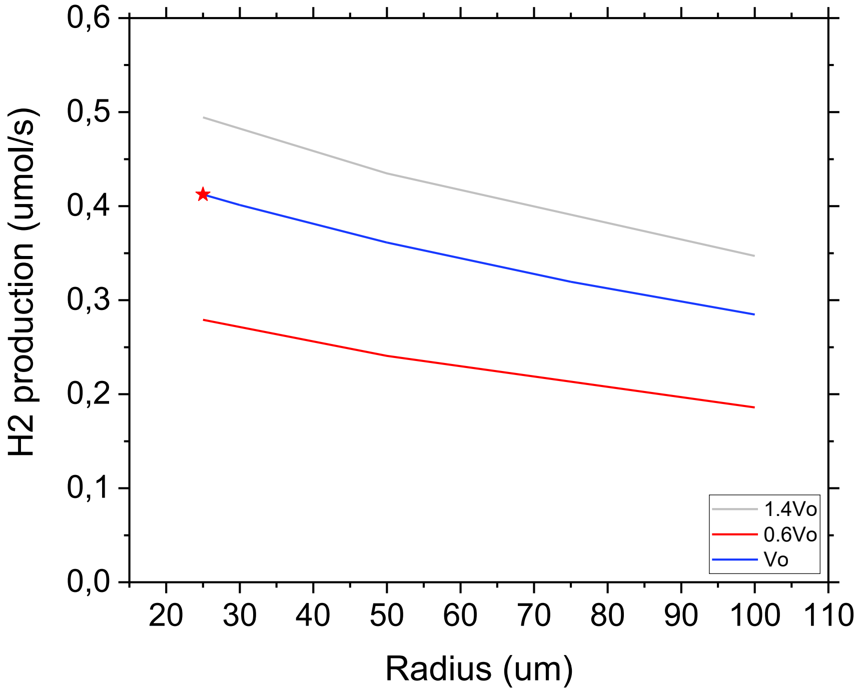

Figure 53-Flow rate dependence for hydrogen production

It was also performed an estimation on the theoretical power produced by a μ-SOFC supplied with the reformed gas flow. It was supposed an efficiency of 100%, as if all the reformed fuel was converted in power by the cell. The useful reformed products were hydrogen (H_2), methane (CH_4) and carbon monoxide (CO). For the estimation of the power were considered the following molar Gibbs free energies:

Table 10- *Molar Gibbs free energies*

Specie	*molar Gibbs free energy (kJ/mol)*
H_2	237
CH_4	140
CO	205.5

Then, each energy was multiplied by each reformed molar flow and summed up as follow:

$$W_{el} = \Delta g_{H_2} \cdot \dot{n}_{H_2} + \Delta g_{CH_4} \cdot \dot{n}_{CH_4} + \Delta g_{CO} \cdot \dot{n}_{CO}$$

The results are reported in Figure 54. It was performed an estimation on various values of the flow rate and for two different lengths of the channel. In the experimental case, the produced power was 0.12 W. However, the biggest improvement was detected by doubling the length of the channel.

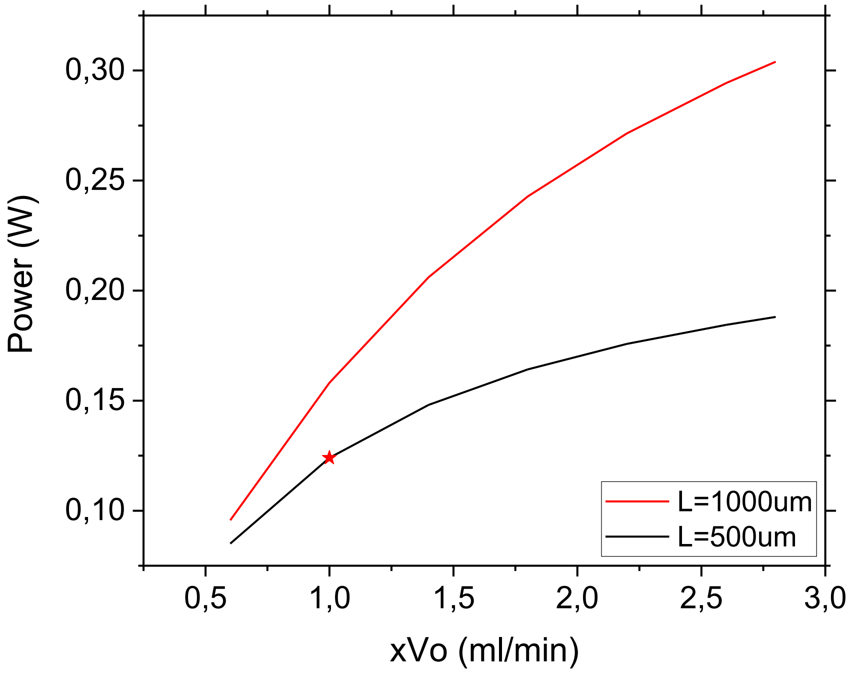

Figure 54- Power evaluation

It was also performed an optimization analysis based on varying the DME/steam ratio. The results are shown in Figure 55. The H2 production is enhanced by increasing the DME/steam ration to 1:6, in the experimental case the ratio was of 1:3. By increasing the quantity of steam is possible to achieve a slightly higher production of hydrogen that is translated in more power production.

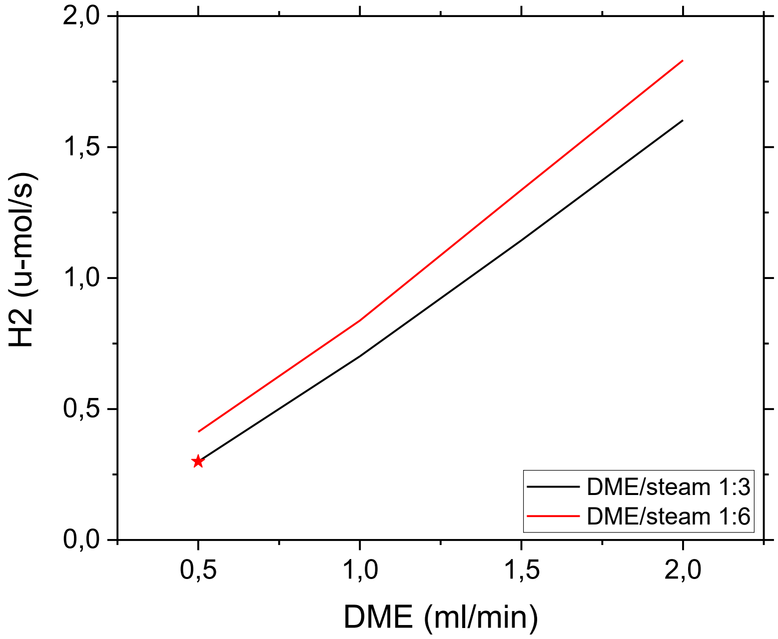

Figure 55- DME/steam ratio comparison for H_2 production

Using the 1:6 ratio, the percentual gain is higher for lower DME flow rate (almost 30 %) and is decreasing with the increase of the DME inflow till a 13 %. Especially for higher flow rate is not one of the most relevant optimization results, but however lead to an increment of power produced.

Table 11-*H2 production in function of DME/steam ratio*

DME Flow rate (ml/min)	*DME/steam 1:6 (µmol/s)*	*DME/steam 1:3 (µmol/s)*	*Percentual gain with 1:6 ratio (%)*
0.5	*0.41*	*0.30*	*27.41*
1	*0.84*	*0.70*	*16.25*
1.5	*1.34*	*1.14*	*14.38*
2	*1.83*	*1.60*	*12.47*

Finally, the increase of the channel length positively affected both DME conversion and H_2 production. The radius dependence showed a maximum for DME conversion that is not technologically achievable, however the results obtained with the 25 µm radius were good. The hydrogen production showed a trend inversely proportional to the increase of the radius dimension. The increase of flow rate led to an increase of hydrogen production but to a decrease of DME conversion, and vice versa. Since H_2 production and power are directly proportional, it may be preferred an increase of flow rate values. As final result, the increase of the DME/stem ration from 1:3 to 1:6 showed a slightly improvement for the production of hydrogen especially for lower DME flow rate.

6 CONCLUSIONS

The present work was dedicated to characterize, understand and improve the performances of the Si-based self-heated µ-reformer. The study was focused on the analysis of the steady-state and start-up conditions of the device and the possible implementation in the micro-power generator. The Si-based µ-reformer has been successfully manufactured by microfabrication process and important novelties have been successfully implemented. The device is composed by a high number of microchannels, internally covered by an ALD deposited Alumina/Pt catalyst, in order to provide a large active area. Furthermore, the device is equipped with a micro-heater element that is able to heat the catalyst at the desired temperature for reforming dimethyl ether.

First, the thermal behaviour of the self-heating µ-reformer was investigated by in-situ Raman spectroscopy measurements. The analysis performed showed that it is suitable for fast start-up processes and dynamic operation. Indeed, the time elapsed between two different measurement (thus two different applied powers) was short and was followed by a quick response of the device. The calibration highlighted also one of the most important results, the maximum reached temperature in the self-heating condition was above 700 °C (when ideal insulation was applied), as also demonstrated by the thermal simulation model. These good results were obtained even with a slightly damaged heater, the gold layer was peeled in some areas. It was noticed that the alumina support, deposited by ALD, caused a mechanical stress on the heater that led to delamination of the gold layer. However, the main role of gold was the protection of the metallic layers deposited underneath. The tungsten layer was always present and it could fulfil its conducting role.

The chemical behaviour of the self-heating µ-reformer was studied by feeding to the system DME and air and measuring the reformed product by a micro GS. The experiment carried out showed a good selectivity of hydrogen (about 12%) and carbon monoxide (about 62%) highlighting the possibility of implementation of this component in the micro-power generator.

Finally, the chemical and thermal behaviour of one micro channel of the micro reformed was simulated by FEM method. The experimental-based simulation model presented a good description of the dimethyl ether steam reforming experiment. The solution resulted grid independent by choosing a number of nodes of almost 2000 and the uncertainty about the activation energies of the reactions was about 10%. The geometry of the system was then varied in order to propose possible optimization in the design. It was observed that the increase of the channel length showed a benefit in both DME conversion and hydrogen production. It is a reasonable result since the more the length increases, the more catalyst is present in the channels. By doubling the length to 1000 µm, the DME conversion overcomes the 90% at 650 °C, against the 75% conversion registered with 500 µm. According to the increase of the channel length, the produced power increased significantly. By doubling both length and entering flow rate the power produced increased from 0.17 W to 0.26 W (considering 100% efficiency of the system). On the other hand, varying the radius of the channels, diffusion and transport mechanisms were affected according to a different trend, leading to a maximum value in DME conversion. The maximum percentage of conversion was reached with a radius of around 5 µm, but is not possible to fabricate such a small channels due to a technological limit. Nevertheless, the DME conversion was not so dissimilar with a radius of 25 µm (about 5% less than the maximum). Regarding flow rate dependences, it affected inversely the two parameters. Increasing flow rate (without changing DME/steam ratio), negatively affected the DME conversion percentage, but increased the hydrogen production, and vice versa. As final result, the DME/steam ratio of 1:6 brought a slight improvement in hydrogen production with respect to the 1:3 ratio used in experimental. The increase was noticed mostly for lower DME flow rate (around 27% more with a DME fed of 0.5 ml/min) and a lower advantage for higher flow rate (around 12% for 2 ml/min fed of fuel).

As future work to improve here presented results, could be the use of a “masking” for the heater when performing the ALD process in order to protect it from peeling. It can be also possible to measure the actual temperature at which the μ-reformer is working for the start-up condition, in order to well characterize the kinetics of the reactions involved. Furthermore, a possible solution can be etching away the Si layer (or a significant part) left in the trench in order to improve the insulation, as the thermal model optimization showed. The average temperature of the central area increased from 740 °C to almost 850 °C, generating a huge thermal gradient with the frame of the sample. In fact, the average frame temperature decreased from 600°C to 480°C. A good insulation allows to reach higher temperature with lower applied power. Finally, the flow rate value can be increased in order to promote the hydrogen production and, as consequence, the power produced.

References

[1] “Personal/Consumer Electronics Market Analysis By Product (Smartphones, Tablets, Desktops, Laptops/Notebooks, Digital Cameras, Hard Disk Drives, E-readers) And Segment Forecasts To 2020.”

[2] “https://batteryuniversity.com/learn/archive/is_lithium_ion_the_ideal_battery”

[3] R. Tian *et al.*, “Quantifying the factors limiting rate performance in battery electrodes,” *Nat. Commun.*, vol. 10, no. 1, 2019, doi: 10.1038/s41467-019-09792-9.

[4] A. Evans, A. Bieberle-Hütter, J. L. M. Rupp, and L. J. Gauckler, “Review on microfabricated micro-solid oxide fuel cell membranes,” *J. Power Sources*, vol. 194, no. 1, pp. 119–129, 2009, doi: 10.1016/j.jpowsour.2009.03.048.

[5] A. Bieberle-h and L. J. Gauckler, “Micro SOFC ONEBAT Project : Battery Replacement using Miniaturized SOFC The Principle of a SOFC SOFC = Solid Oxide Fuel Cell,” pp. 1–25.

[6] A. Evans *et al.*, “Micro-solid oxide fuel cells: Status, challenges, and chances,” *Monatshefte fur Chemie*, vol. 140, no. 9, pp. 975–983, 2009, doi: 10.1007/s00706-009-0107-9.

[7] F. Chiabrera, I. Garbayo, N. Alayo, and A. Tarancón, “Micro solid oxide fuel cells: a new generation of micro-power sources for portable applications,” *Smart Sensors, Actuators, MEMS VIII*, vol. 10246, no. 1, p. 102460S, 2017, doi: 10.1117/12.2269454.

[8] I. Garbayo, M. Salleras, A. Morata, and D. Pla, “Is it possible to design a portable power generator based on micro-solid oxide fuel cells ? A fi nite volume analysis nchez-Gonz a,” vol. 293, pp. 264–273, 2015, doi: 10.1016/j.jpowsour.2015.05.046.

[9] A. M. Abdalla, S. Hossain, E. Commission, A. T. Azad, and F. Begum, “Nanomaterials for solid oxide fuel cells : A review Paper (I) Nanomaterials for solid oxide fuel cells : A review Abdalla M . Abdalla , Shahzad Hossain , Atia T . Azad , Pg Mohammad I . Petra ,” no. February, 2018, doi: 10.1016/j.rser.2017.09.046.

[10] K. J. Kim, B. H. Park, S. J. Kim, Y. Lee, H. Bae, and G. M. Choi, “Micro solid oxide fuel cell fabricated on porous stainless steel : a new strategy for enhanced thermal cycling ability,” *Nat. Publ. Gr.*, no. December 2015, pp. 1–8, 2016, doi: 10.1038/srep22443.

[11] P. Su, C. Chao, J. H. Shim, R. Fasching, and F. B. Prinz, “Solid Oxide Fuel Cell with Corrugated Thin Film Electrolyte 2008,” no. 100, 2008.

[12] A. Cirera, C. Lpez-Gándara, and F. M. Ramos, “YSZ-based oxygen sensors and the use of nanomaterials: A review from classical models to current trends,” *J. Sensors*, vol. 2009, no. Figure 1, 2009, doi: 10.1155/2009/258489.

[13] V. A. Online, I. Garbayo, D. Pla, A. Morata, and L. Fonseca, “Environmental Science Full ceramic micro solid oxide fuel cells : towards more reliable MEMS power generators operating at,” 2014, doi: 10.1039/C4EE00748D.

[14] M. Lo Faro, V. Antonucci, P. L. Antonucci, and A. S. Aricó, “Fuel flexibility: A key challenge for SOFC technology,” *Fuel*, vol. 102, pp. 554–559, 2012, doi: 10.1016/j.fuel.2012.07.031.

[15] D. Creaser, M. Nilsson, L. J. Pettersson, and J. Dawody, “Kinetic modeling of autothermal reforming of dimethyl ether,” *Ind. Eng. Chem. Res.*, vol. 49, no. 20, pp. 9712–9719, 2010, doi: 10.1021/ie100834v.

[16] R. Peters, R. Dahl, U. Klüttgen, C. Palm, and D. Stolten, “Internal reforming of methane in solid oxide fuel cell systems,” *J. Power Sources*, vol. 106, no. 1–2, pp. 238–244, 2002, doi: 10.1016/S0378-7753(01)01039-4.

[17] Y. FUJISHIRO, T. SUZUKI, T. YAMAGUCHI, K. HAMAMOTO, and M. AWANO, “Challenge for the development of micro SOFC manufacturing technology,” *Synth. English Ed.*, vol. 4, no. 1, pp. 45–55, 2011, doi: 10.5571/syntheng.4.45.

[18] D. Pla, "Integration of micro solid oxide fuel cells in power generator devices," *Thesis 2015*, vol. 1, 2015, doi: 10.1017/CBO9781107415324.004.

[19] R. W. Johnson, A. Hultqvist, and S. F. Bent, "A brief review of atomic layer deposition: From fundamentals to applications," *Mater. Today*, vol. 17, no. 5, pp. 236–246, 2014, doi: 10.1016/j.mattod.2014.04.026.

[20] F. M. Chiabrera, "Interface Engineering in Mixed Ionic Electronic Conductor Thin Films for Solid State Devices," 2019.

[21] COMSOL, "https://www.comsol.it/multiphysics/finite-element-method"

[22] A. G. Gayubo *et al.*, "Causes of deactivation of bifunctional catalysts made up of CuO-ZnO-Al 2O3 and desilicated HZSM-5 zeolite in DME steam reforming," *Appl. Catal. A Gen.*, vol. 483, pp. 76–84, 2014, doi: 10.1016/j.apcata.2014.06.031.

[23] Q. Zhang, X. Li, K. Fujimoto, and K. Asami, "Hydrogen production from partial oxidation and reforming of DME," vol. 102, no. August, pp. 0–3, 2005, doi: 10.1007/s10562-005-5855-5.

[24] D. Tuschel, "Raman thermometry," *Spectrosc. (Santa Monica)*, vol. 31, no. 12, pp. 8–13, 2016.

[25] "halas.rice.edu/conversion"

[26] G. S. Doerk, C. Carraro, and R. Maboudian, "Temperature dependence of Raman spectra for individual silicon nanowires," *Phys. Rev. B - Condens. Matter Mater. Phys.*, vol. 80, no. 7, pp. 1–4, 2009, doi: 10.1103/PhysRevB.80.073306.

[27] A. Marini, "Parametri Elastici E," pp. 1–10, 2009.

[28] Y. Chen and Z. Shao, "Partial oxidation of dimethyl ether to H 2 / syngas over supported Pt catalyst," vol. 17, no. 20060400928, pp. 75–80, 2008.

[29] K. Takeishi and H. Suzuki, "Steam reforming of dimethyl ether," *Appl. Catal. A Gen.*, vol. 260, no. 1, pp. 111–117, 2004, doi: 10.1016/j.apcata.2003.10.006.

[30] F. A. Elewuwa and Y. T. Makkawi, "Hydrogen production by steam reforming of DME in a large scale CFB reactor. Part I: Computational model and predictions," *Int. J. Hydrogen Energy*, vol. 40, no. 46, pp. 15865–15876, 2015, doi: 10.1016/j.ijhydene.2015.10.050.

[31] P. F. GAY and T. MORRIS W., "ON THE THERMAL DECOMPOSITION OF DIMETHYL ETHER," pp. 756–770, 1937.

[32] L. C. Almeida, O. Sanz, D. Merino, G. Arzamendi, L. M. Gandía, and M. Montes, "Kinetic analysis and microstructured reactors modeling for the Fischer-Tropsch synthesis over a Co-Re/Al2O3 catalyst," *Catal. Today*, vol. 215, pp. 103–111, 2013, doi: 10.1016/j.cattod.2013.04.021.

[33] M. K. Nikoo and N. A. S. Amin, "Thermodynamic analysis of carbon dioxide reforming of methane in view of solid carbon formation," *Fuel Process. Technol.*, vol. 92, no. 3, pp. 678–691, 2011, doi: 10.1016/j.fuproc.2010.11.027.

[34] P. properties of H. Gallant., H. C. E. Perri., and S. T. P. of G. and L. T. I. C. I. Reid, Prausnitz, "Diffusività dei Gas Gas / Vapore Gas / Vapore," pp. 1–6.

Acknowledgments

First of all, I want to thank my thesis supervisors Francesco, Nerea and Marco for all the helps, advices and everything they've taught me. You have made my first lab experience unforgettable. Thanks Francesco for all your time spent with me, I've learned a lot from you. I enjoyed all the time spent in the lab together and also all the time spent trying to make the model work. Nerea, thanks for giving me the opportunity to enter a cleaning room, it was amazing. The last but not the least, thanks Marco for all your CADs and images that you made for me and my work. I appreciated the great assistance that you all provided during my work. It has been a pleasure to work with you.

I want to express my deepest gratitude to my thesis tutor from the Politecnico, prof. Smeacetto. Without him, I couldn't have done one of the most beautiful experience of my life. Thanks also for your availability and kindness for all the administrative matters and throughout the work.

Of course, I loved this experience also thanks to all of my colleagues of IREC. Thank you Albert and Alex for listening to me the Monday morning and giving me advices to continue the work. Thanks Mar, Maritta, Juande, Jose, Federico, Simone, Paolo, Marina, Carolina, Gotzon, Lucille, Natalia, Arianna, Valerie, Aitor, Julian, Merce, Marc T., Marc N., Yunqing, Zerrin for each coffee break, lunch, beer and also for each discussion and complaints about food and coffee. You made me feel comfortable and I enjoyed each moment spent with you. This experience was that beautiful also because of you.

Grazie a tutti gli amici conosciuti a Torino, avete reso questo percorso bellissimo e indimenticabile. Abbiamo condiviso tanto tempo, tante esperienze e tante emozioni insieme. Grazie agli amici di sempre di Salemi, che anche a distanza ci sono sempre stati e hanno sempre gioito e festeggiato con me.

Grazie a Dario, compagno di studio, di vita e di avventure. Un percorso iniziato e finito insieme, dal primo all'ultimo giorno, dal primo all'ultimo esame. In questi 5 anni trascorsi insieme sei diventato come un fratello per me, grazie per esserci sempre stato e per avermi aiutato in tutto.

Grazie a tutta la mia famiglia per avermi sempre supportato, sollevandomi l'animo nei periodi di difficoltà e gioendo per me nei momenti di felicità anche con delle semplici chiamate. Siete sempre riusciti a strapparmi una risata e rendere tutto più bello. Vi voglio bene.

Grazie a voi, Anna, Ninni e Clodz. Grazie per essermi sempre stati vicino anche da lontano, per avermi sempre sostenuto nel bene e nel male, per aver sempre creduto in me dall'inizio alla fine. Siete stati e sarete la mia forza più grande. Grazie per tutto quello che mi avete dato e insegnato, non avrei mai potuto affrontare tutto questo senza voi. Senza voi non sarei l'uomo che sono diventato. Siete speciali.